Supplementary Information for:

Structural Properties of Ultra-Small Thorium and Uranium Dioxide Nanoparticles Embedded in a Covalent Organic Framework

Liane M. Moreau,[1‡] Alexandre Herve,[1‡] Mark D. Straub,[1,2] Dominic R. Russo,[1,2] Rebecca J. Abergel,[1,2] Selim Alayoglu,[1] John Arnold,[1,2] Augustin Braun,[1] Gauthier J.P. Deblonde,[1,3] Yangdongling Liu,[1] Trevor D. Lohrey,[1,2] Daniel T. Olive,[1,4] Yusen Qiao,[1,5] Julian A. Rees,[1] David K. Shuh,[1] Simon J. Teat,[1] Corwin H. Booth,[1]* Stefan G. Minasian[1]*

[1] *Lawrence Berkeley National Laboratory, Berkeley, CA 94720, United States*

[2] *University of California, Berkeley, CA 94720, United States*

[3] *Lawrence Livermore National Laboratory, Livermore, CA 94550, United States*

[4] *Los Alamos National Laboratory, Los Alamos, NM 87545, United States*

[5] *University of Pennsylvania, Philadelphia, PA 19104, United States*

‡ These authors contributed equally

Email: chbooth@lbl.gov, sgminasian@lbl.gov

Table of Contents:

Extended Methods

Single Crystal X-ray Diffraction. Single-crystal diffraction data for $Th(hfa)_4(dme)$ and $U(hfa)_4$ were collected using synchrotron radiation at the Advanced Light Source at Lawrence Berkeley National Laboratory on beamline 11.3.1 (λ = 0.7749 Å). Single crystals were selected and sized using a microscope outfitted with a polarizing filter. Once selected, the paratone-coated crystals were mounted onto 10 micron MiTiGen Dual-Thickness MicroLoops, transferred immediately to the goniometer head, and cooled by a 100 K dry nitrogen stream. Diffraction data were collected at the Advanced Light Source station 11.3.1, using a 16 keV (λ = 0.7749 Å) beam of silicon-monochromated synchrotron radiation and a Bruker D8 with PHOTON 100 detector. The Bruker APEX3 software package and its associated programs (e.g. SAINT, SADABS) were used for the data collection, unit cell determination and refinement, integration, and absorption correction procedures.[1] Initial structure solutions were determined using SHELXT and structure refinements (against F^2) were conducted using SHELXL-2014 within the WinGX software package.[2, 3] Thermal parameters for all non-hydrogen atoms were refined anisotropically. Discussion of the structural refinements can be found below in conjunction with Figures S1 and S2. ORTEP diagrams were created using the ORTEP-3 software package and POV-Ray.[3] A summary of the X-ray diffraction data is presented in Tables S1 and S2. Structures have been deposited to the Cambridge Crystallographic Data Centre, with deposition numbers **1952481** (for $Th(hfa)_4(dme)$) and **1952482** (for $U(hfa)_4$). These data may be obtained free-of-charge at https://www.ccdc.cam.ac.uk/.

The crystal structure [$Th(hfa)_4(dme)$], as solved in the monoclinic space group C2/c, indicated a case of complete whole molecule disorder, with Th occupying a site of 2-fold symmetry (Figure S1 and Table S1). The whole molecule disorder was observed even when the data was integrated and solved in a primitive cell, indicating that the C-centering was not the cause of the apparent disorder of the ligands. Due to the high quality of the data obtained using the synchrotron, all non-H atoms could be located and refined anisotropically. A mild ISOR restraint was necessary for several non-H atoms to yield reasonable thermal ellipsoids. On the basis of several refinements with a freely refined free variable, all atoms were eventually refined at a fixed 50% occupancy to account for the whole molecule disorder.

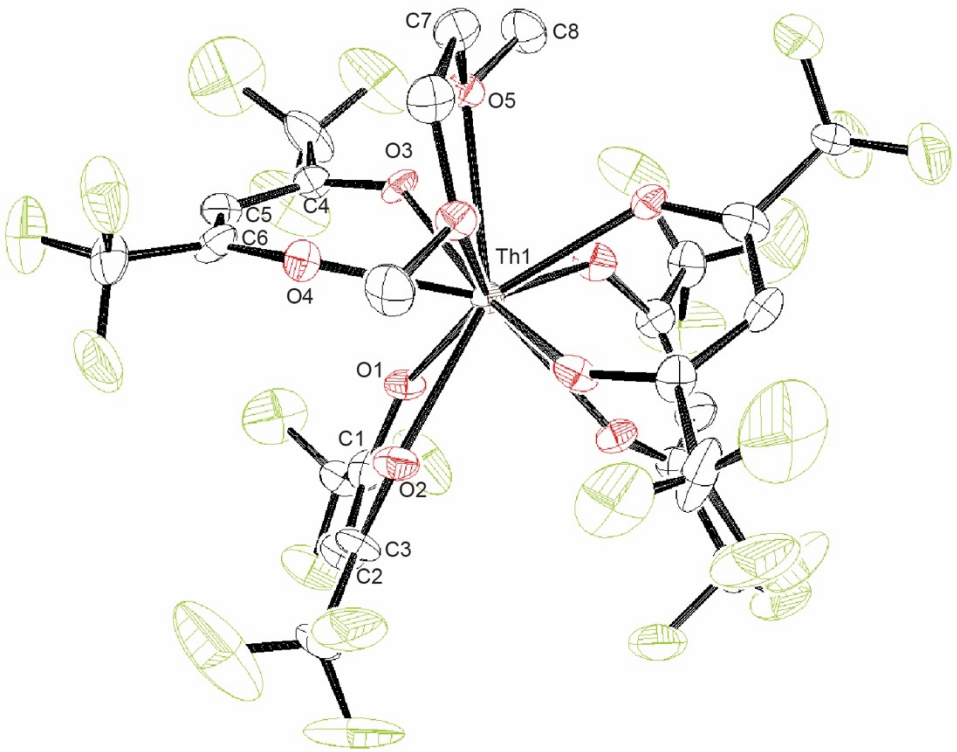

Figure S1. Molecular structure of $Th(hfa)_4(dme)$. Thermal ellipsoids are drawn at the 50% probability level. Hydrogen atoms have been removed for clarity. Because the structure exhibited whole molecule disorder, only one set of hfa and dme ligands is shown.

Table S1. Selected Bond Lengths (Å) and Angles (deg) for $Th(hfa)_4(dme)$.

Atoms	Bond Lengths (Å)	Atoms	Bond Angles (deg)
Th(1)–O(1)	2.403(10)	O(1)–Th(1)–O(2)	70.6(2)
O(1)–C(1)	1.271(13)	Th(1)–O(1)–C(1)	136.7(8)
C(1)–C(2)	1.371(12)	O(1)–C(1)–C(2)	128.5(9)
C(2)–C(3)	1.41(2)	C(1)–C(2)–C(3)	120.1(11)
C(3)–O(2)	1.291(19)	C(2)–C(3)–O(2)	129.1(14)
Th(1)–O(2)	2.457(2)	C(3)–O(2)–Th(1)	132.9(8)
Th(1)–O(3)	2.542(17)	O(3)–Th(1)–O(4)	66.9(5)
O(3)–C(4)	1.21(2)	Th(1)–O(3)–C(4)	133.2(9)
C(4)–C(5)	1.380(17)	O(3)–C(4)–C(5)	127.0(14)
C(5)–C(6)	1.37(2)	C(4)–C(5)–C(6)	120.5(12)
C(6)–O(4)	1.354(19)	C(5)–C(6)–O(4)	127.4(15)
Th(1)–O(4)	2.394(17)	C(6)–O(4)–Th(1)	135.5(12)

Solving the $[U(hfa)_4]$ structure in the tetragonal space group I41/a revealed two separate molecules, with one uranium (U1) sitting on a -4 axis, with one crystallographically independent hfa ligand and the other uranium (U2) occupying a 2-fold axis, with two crystallographically independent hfa ligands (Figure S2 and Table S2). The structural model for two of the three independent hfa ligands (containing O1, O2, O3, and O4) required no restraints, while the third

hfa ligand (containing O5 and O6) required a mild ISOR restraint be applied to several carbon atoms to yield reasonable thermal parameters. Based on the Goodness-of-Fit (S), application of this restraint was not unduly applied and in line with the electron density in this region being rather dispersed. No positional disorder was modeled for any atoms, including the fluorine atoms, which do display some degree of fluxionality due to poor intermolecular interactions between highly fluorinated molecules.

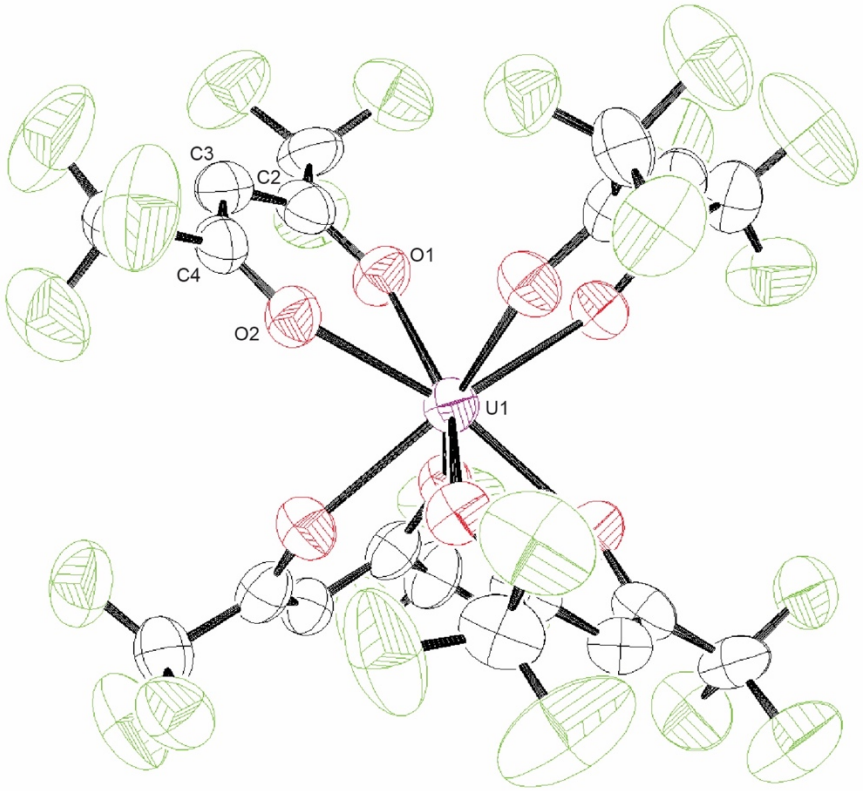

Figure S2. Molecular structure of $U(hfa)_4$. Thermal ellipsoids are drawn at the 50% probability level. Hydrogen atoms have been removed for clarity.

Table S2. Selected Bond Lengths (Å) and Angles (deg) for $U(hfa)_4$.

Atoms	Bond Lengths (Å)	Atoms	Bond Angles (deg)
U(1)–O(1)	2.297(7)	O(1)–U(1)–O(2)	70.2(2)
O(1)–C(2)	1.277(14)	U(1)–O(1)–C(2)	140.8(7)
C(2)–C(3)	1.394(15)	O(1)–C(2)–C(3)	125.0(11)
C(3)–C(4)	1.394(15)	C(2)–C(3)–C(4)	119.7(11)
C(4)–O(2)	1.263(13)	C(3)–C(4)–O(2)	127.5(10)
U(1)–O(2)	2.366(7)	C(4)–O(2)–U(1)	136.6(7)

Table S3. Crystal Data and Structure Refinement Details

	$U(HFA)_4$	**$Th(HFA)_4(DME)$**
Chemical formula	$C_{20}H_4F_{24}O_8U$	$C_{24}H_{14}F_{24}O_{10}Th$
Formula weight	1066.26	1150.39
Color, habit	Orange, block	Colorless, shard
Temperature (K)	100(2)	100(2)
Crystal system	Tetragonal	Monoclinic
Space group	$I4_1/a$	$C2/c$
a (Å)	17.4457(4)	12.8993(5)
b (Å)	17.4457(4)	15.9751(7)
c (Å)	29.8629(9)	17.3394(7)
α (°)	90	90
β (°)	90	97.371(3)
γ (°)	90	90
V ($Å^3$)	9088.8(5)	3543.6(3)
Z	12	4
Density (Mg m^{-3})	2.338	2.156
F(000)	5952	2176
Radiation Type	Synchrotron	Synchrotron
μ (mm^{-1})	3.108	2.472
Crystal size	0.05 x 0.03 x 0.02	0.07 x 0.01 x 0.01
Meas. Refl.	39526	17900
Indep. Refl.	4162	4079
R(int)	0.0829	0.0560
Final R indices	R = 0.0543	R = 0.0296
[I > 2σ(I)]	R_w = 0.1361	R_w = 0.0536
Goodness-of-fit	1.016	1.073
$\Delta\rho_{max}$, $\Delta\rho_{min}$ (e $Å^{-3}$)	2.614, -1.265	1.855, -1.216

X-ray scattering data and fitting results

Small and wide-angle x-ray scattering of pure COF-5, inclusion compounds and nanoparticles were collected and are shown below.

X-ray scattering data collection and fitting details

In order to understand the details behind fitting methods, sample acquisition conditions are outlined below. Due to the radioactive nature of the samples, a containment configuration (Fig. S3) was required. Powder samples were diluted with boron nitride, placed into quartz capillaries, and those quartz capillaries placed into kapton capillaries sealed with epoxy. The kapton capillaries were then taped into an aluminum holder with kapton windows. It should be noted that non-radioactive samples were measured in a separate holder without kapton windows. For each holder, calibration and sample-to-detector distance was determined using a silver behenate standard.

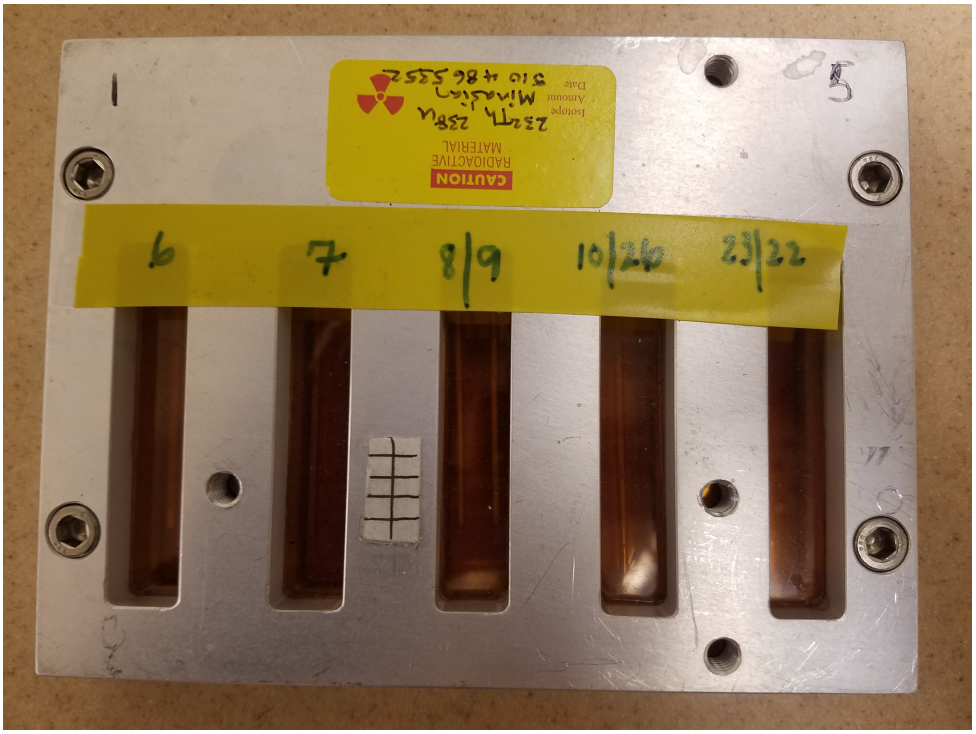

Figure S3: SAXS sample containment. The holder used for radioactive samples is made of aluminum with kapton windows. Inside of the holder, samples in quartz capillaries inside of outer kapton capillaries are taped into slots.

Standard scattering patterns are shown in Figure S4 (with the exception of the COF-5 standard, which is shown in Figs. S5 and S6). It should be clarified that while the “kapton” sample was purely a kapton tube, the “quartz” standard was an empty capillary within a kapton tube. The

"boron nitride" standard was boron nitride powder packed into a quartz capillary placed inside of a kapton tube. The "COF-5" and inclusion compound standards were also mixed with boron nitride and placed inside of quartz capillaries and kapton tubes. Thus, it should be taken into account that the standard samples also have containment. This was considered when choosing which standards were to be included in the fits (Figs. S5a and S6a).

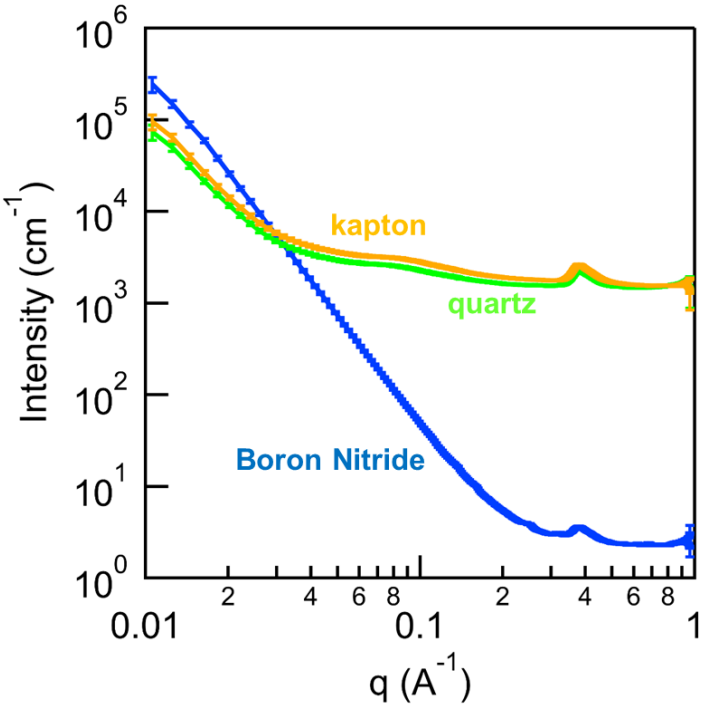

Figure S4: Standard SAXS patterns. Kapton, quartz (in kapton) and boron nitride (in quartz and kapton) standard patterns are shown. Each of these represent layers of containment present in the inclusion compound and nanoparticle samples.

Given that the thickness of the kapton tubes and quartz capillaries is relatively constant between samples, for the nanoparticle samples, the standards fit in linear combination with a spherical form factor integrated over a Schultz distribution were boron nitride, COF-5 and the relevant inclusion compound. The inclusion compound was chosen as a standard given the trend noted from both PXRD and WAXS that upon pore occupancy in COF-5 with the inclusion compound, the first order reflections become inverted and so this was required as a standard in order to achieve a quality fit in the WAXS region. Additionally, a different type of kapton was used on the radioactive holder than in the kapton tubes in the non-radioactive standards as can be observed around ~0.4 Å^{-1} in q, and this is captured in the inclusion compound background as well. This being said, if kapton is substituted for the inclusion compound in the fits as a standard,

while the fitting statistics are not as good (χ^2 = 57 vs. χ^2 = 14), the resulting nanoparticle radius and polydispersity are similar, indicating that it is the WAXS region that is primarily improved by having the inclusion compound as a background in the fitting procedure.

From taking the analytical solution to a spherical form factor integrated over a Schultz distribution $(F(q))^4$ and fitting this in linear combination with relevant standards, the following was used to fit the nanoparticle SAXS patterns, where z is related to the polydispersity according to

Polydispersity = $\frac{100}{\sqrt{z+1}}$

and r_p is the radius of the nanoparticle.

I(q) = A*F(q) + B*[COF-5 background (q)] + C*[BN background (q)] + D*[inclusion compound background (q)]

Using this method, the best-fit values of r_p, z, A, B, C and D for the UO_2 NPs@COF-5 and ThO_2 NPs@COF-5 were extracted.

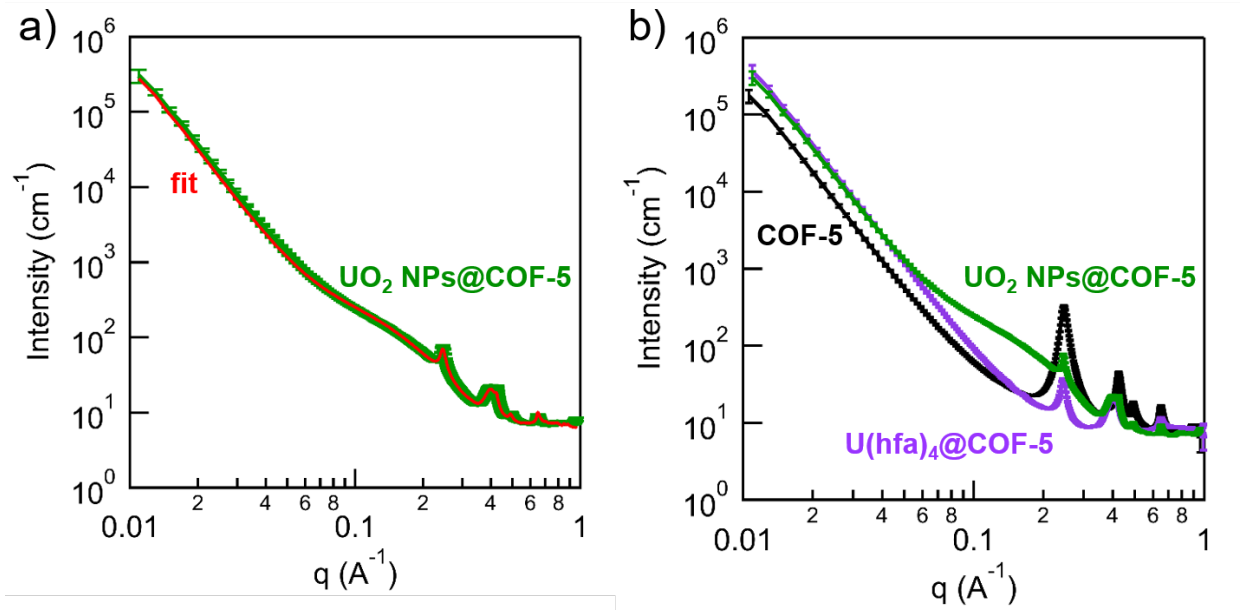

Figure S5: UO_2 NPs@COF-5 SAXS data and fit. a) The fit (red) well matches the SAXS pattern of UO_2 NPs@COF-5 (green). b) The curvature observed above 0.06 $Å^{-1}$ is only present in the nanoparticle sample (green). The COF-5 peaks in the WAXS region are observed also in the $U(hfa)_4$@COF-5 and UO_2 NPs@COF-5 samples.

Table S4: Results from best-fit model for UO_2 NPs@COF-5

Parameter	Best-fit value	χ^2
z	3.3 ± 0.4	14.0
r_p	6.8 ± 0.3 Å	
A	0.00109 ± 0.00009	
B	0.053 ± 0.004	
C	-0.07 ± 0.05	
D	0.78 ± 0.02	

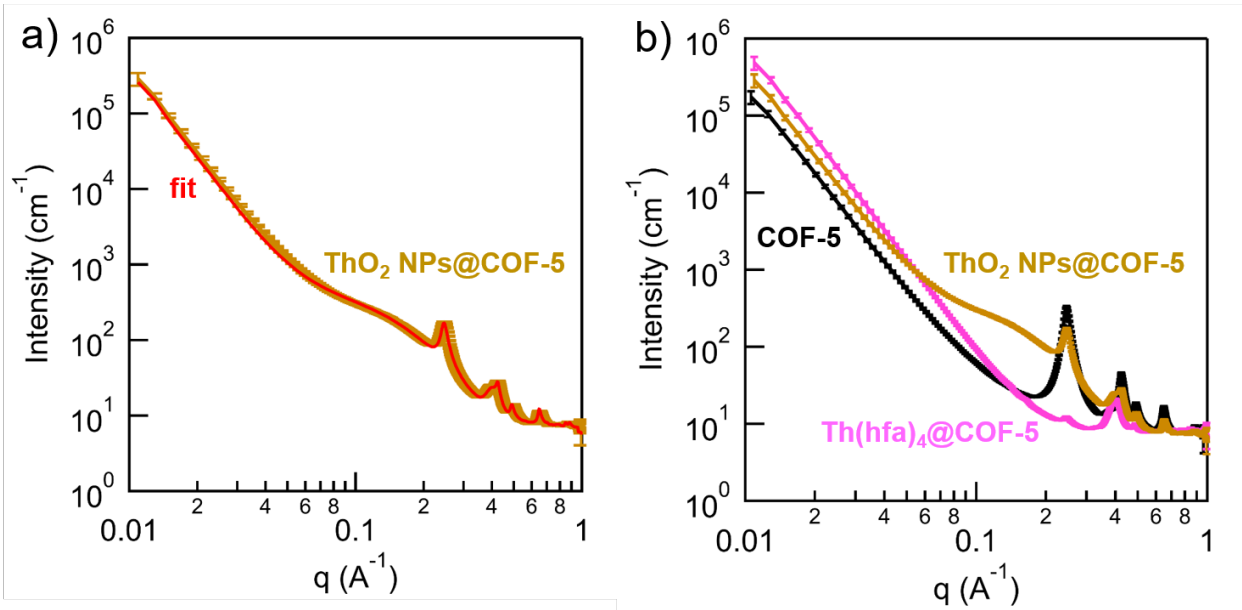

Figure S6: ThO_2 NPs@COF-5 SAXS data and fit. a) The fit (red) well matches the SAXS pattern of UO_2 NPs@COF-5 (tan). b) The curvature observed above 0.06 Å^{-1} is only present in the nanoparticle sample (tan). The COF-5 peaks in the WAXS region are observed also in the Th(hfa)$_4$@COF-5 and ThO_2 NPs@COF-5 samples.

Table S5: Results from best-fit model for ThO_2 NPs@COF-5

Parameter	Best-fit value	χ^2
z	6.4 ± 0.4	6.3
r_p	8.1 ± 0.1 Å	
A	0.00124 ± 0.00004	
B	0.375 ± 0.004	
C	-0.71 ± 0.04	
D	0.73 ± 0.01	

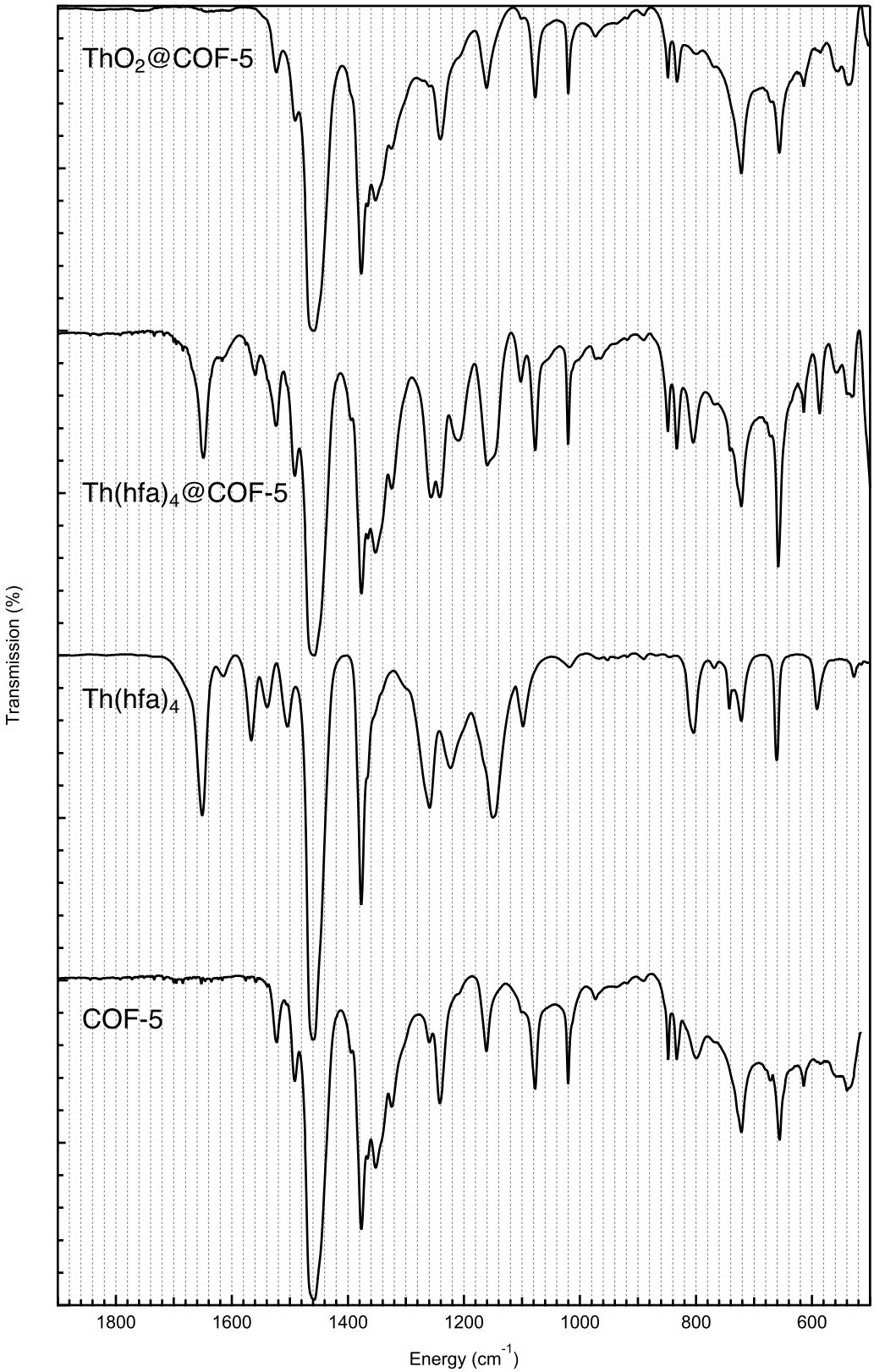

Figure S7. Complete IR spectra for COF-5, $Th(hfa)_4$, $Th(hfa)_4$@COF-5, and ThO_2 NPs@COF-5.

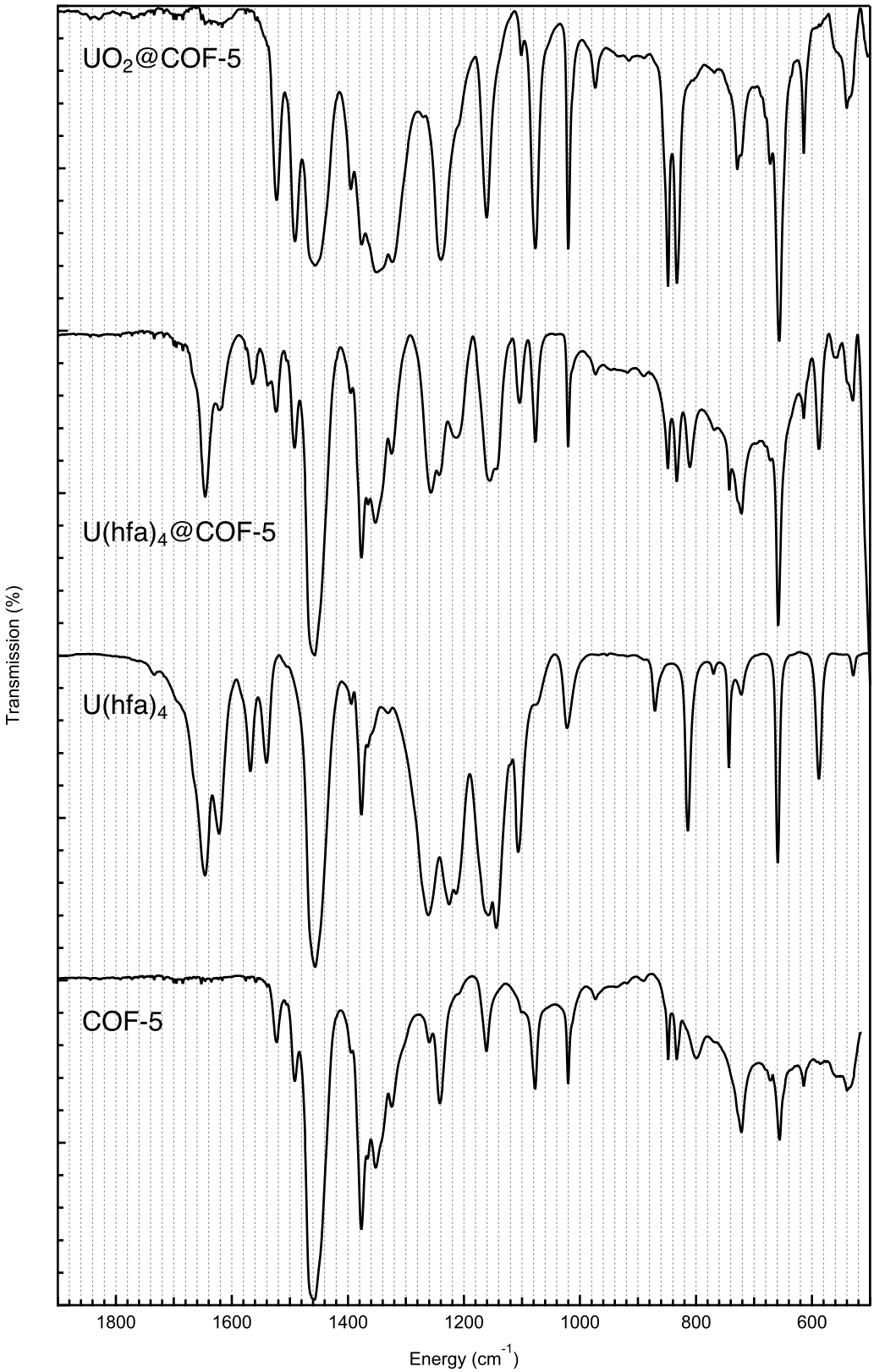

Figure S8. Complete IR spectra for COF-5, $U(hfa)_4$, $U(hfa)_4$@COF-5, and UO_2 NPs@COF-5.

Table S6. IR frequencies and proposed assignments. Where available, assignments are adapted from literature references.[5, 6]

$Th(hfa)_4$	$U(hfa)_4$	COF-5	$Th(hfa)_4$ @COF-5	$U(hfa)_4$ @COF-5	ThO_2 NPs @COF-5	UO_2 NPs @COF-5	Proposed Assignments
I. Transitions associated with hexafluoroacetylacetonate ligands							
528	529		531	530			v(M-O) stretch
592	589		587	589			v(M-O) stretch + v(C-CF_3) bend
742	742		741	742			v(C-CF_3) stretch
804	805		805	810			v(C–H) out of plane
1098	1100		1102	1104			unassigned
1144	1144		1143	1144			v(C-H) in plane bend
1153	1154		1152	1155			v(C-H) in plane bend
1223	1206		1209	1213			v(C-C) stretch
1539	1534		1536	1539			v(C-C) stretch
1566	1560		1560	1564			v(C-H) in plane bend?
1615	1612		1617	1621			v(C=O) + v(C=C)
1651	1650		1649	1646			v(C=O) + v(C=C)
	1670			1669			v(C=O)
II. Transitions associated with COF-5							
		614	614	614	614	614	v(C–H) out of plane
		799	not obs.	not obs.	799	not obs.	v(C–H) out of plane
		833	833	833	833	833	v(C–H) out of plane
		848	848	848	848	848	v(C–H) out of plane
		973	973	973	973	974	v(C=C)
		1020	1020	1020	1020	1020	v(B–C)
		1077	1077	1077	1077	1077	v(C–H) in plane
		1161	1161	1161	1161	1161	v(C–H) in plane
		1242	1242	1243	1241	1240	v(C–O)
		1324	1325	1325	1325	1324	v(C–O)
		1352	1352	1352	1352	1350	v(B–O)
		1492	1492	1492	1491	1491	v(C=C)
		1523	1524	1523	1523	1523	v(C=C)

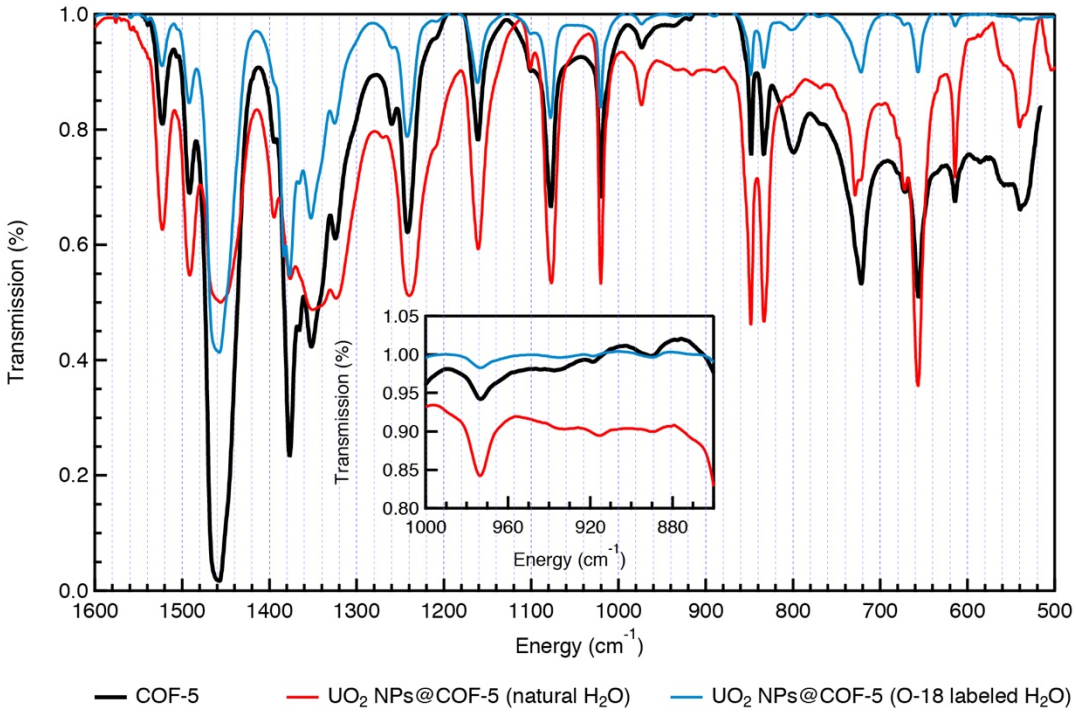

Figure S9. Plot comparing the IR spectra of samples of UO_2 NPs@COF-5 that were prepared by decomposing $U(hfa)_4$@COF-5 in the presence of unlabelled H_2O (red) and with 18-O labeled H_2O (blue). A reference spectrum of COF-5 is also provided (black). No significant differences are observed in the two UO_2 NPs@COF-5 spectra, indicating that the spectra are dominated by transitions associated with COF-5.

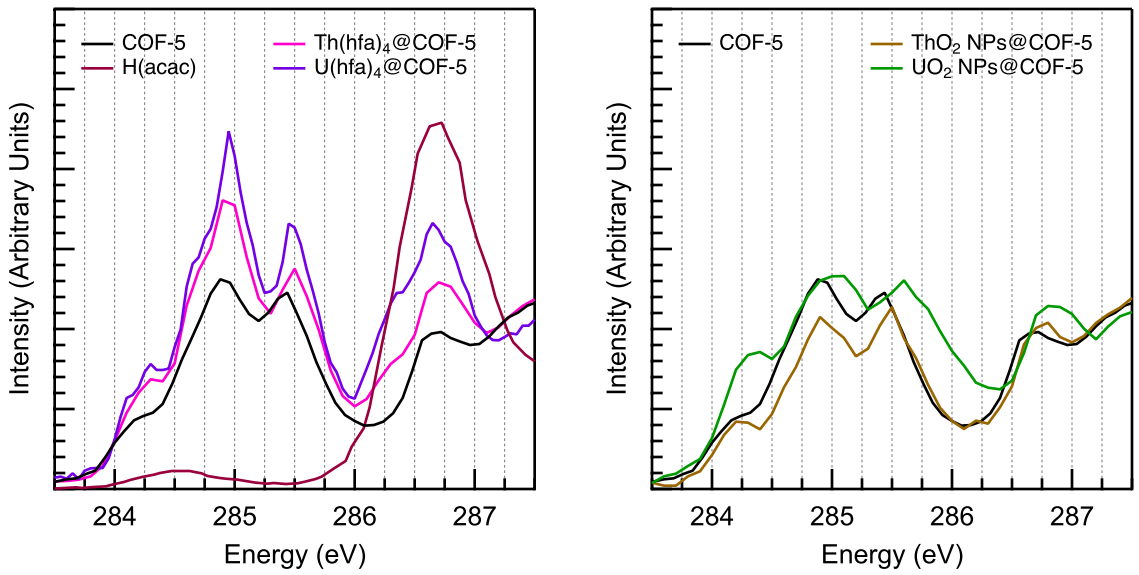

Figure S10. Left, comparison of carbon K-edge XAS data for $Th(hfa)_4$@COF-5 and $U(hfa)_4$@COF-5 with COF-5 and acetylacetone, H(acac). Right, comparison of carbon K-edge XAS data for ThO_2 NPs@COF-5 and UO_2 NPs@COF-5 with COF-5. The spectrum of acetylacetone is adapted with permission from Lessard et al.[7]

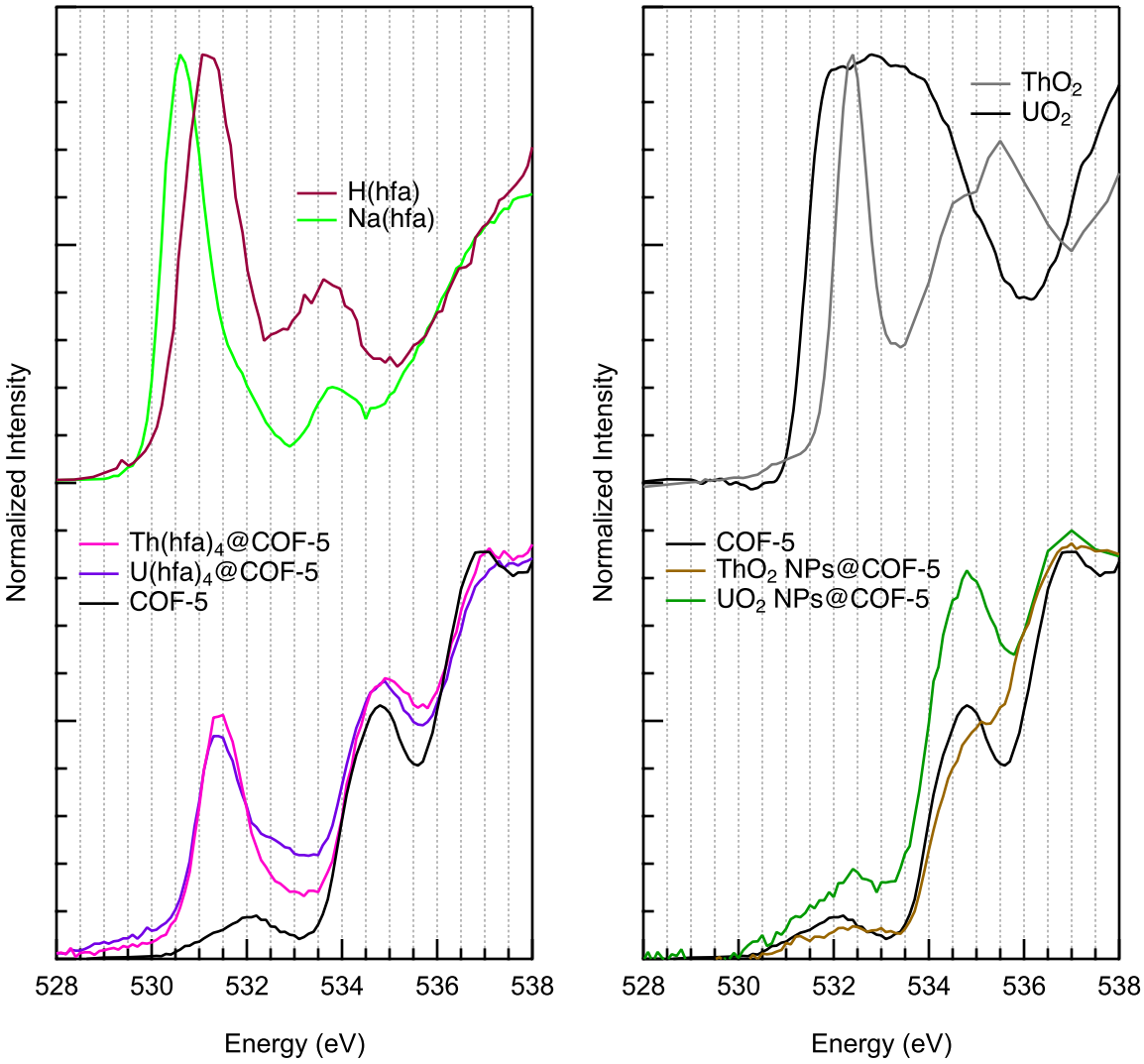

Figure S11. Left, comparison of oxygen K-edge XAS data for $Th(hfa)_4$@COF-5 and $U(hfa)_4$@COF-5 with COF-5, Na(hfa), and acetylacetone, H(acac). Right, comparison of oxygen K-edge XAS data for ThO_2 NPs@COF-5 and UO_2 NPs@COF-5 with COF-5, ThO_2, and UO_2. The spectrum of acetylacetone is adapted with permission from Lessard et al.[7]

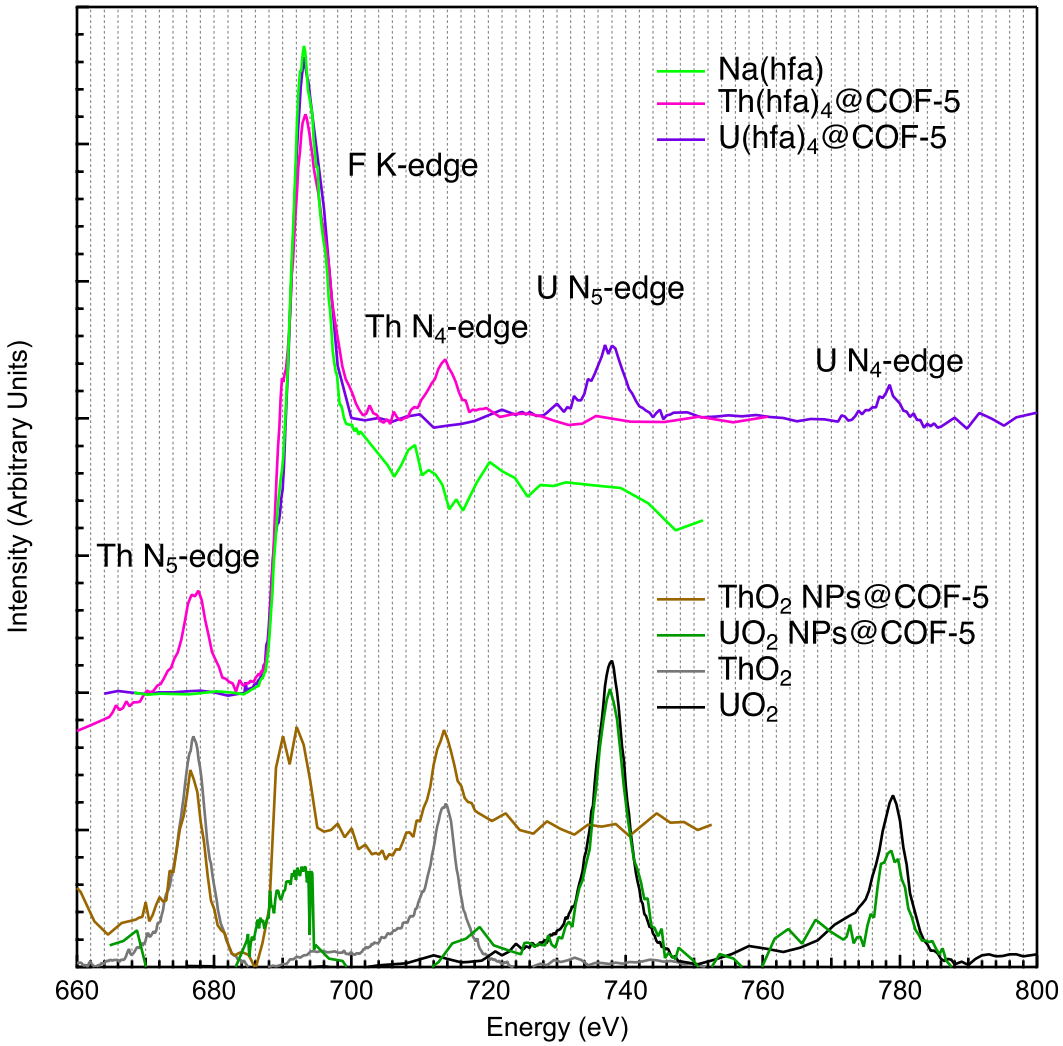

Figure S12. Comparisons of the F K-edge, Th $N_{5,4}$-edge, and U $N_{5,4}$-edge XAS data for $Th(hfa)_4$@COF-5, $U(hfa)_4$@COF-5, ThO_2 NPs@COF-5, and UO_2 NPs@COF-5 with Na(hfa), ThO_2, and UO_2. The F K-edge is convoluted with the Th $N_{5,4}$-edge and U $N_{5,4}$-edge and spectral normalizations are approximate. Spectra have been scaled to show the correspondence in energy between edges measured for different datasets.

Supplementary L_3 Edge X-Ray Absorption Fine Structure Data

EXAFS data and fitting results

EXAFS fitting models along with derived parameters and goodness of fit statistics are shown below, along with the *k* and *r*-ranges used for each sample fit. All fits were performed in *r*-space. It should be noted that the reported E_0 values, although quite large in magnitude, are in line with what has been reported for actinide systems previously[8] and can be attributed to a Femi level error in FEFF.

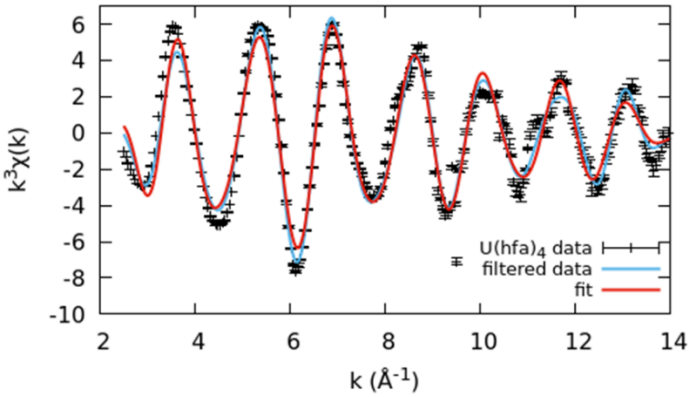

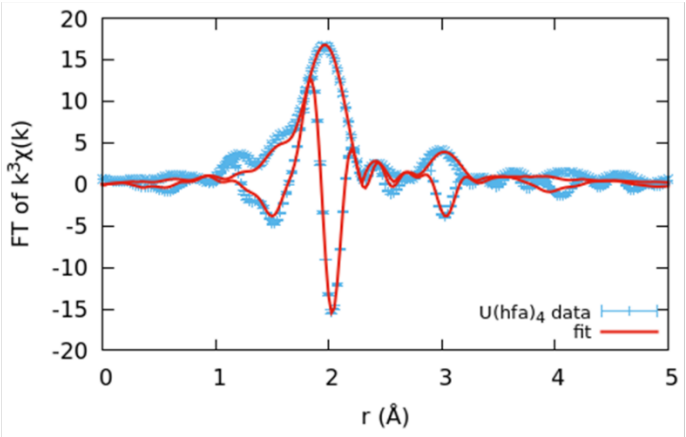

Sample	Path	*N*	*R* (Å)	σ^2 (Å^2)	ΔE_0 (eV)
$U(hfa)_4$ precursor	U-O	8	2.382(6)	0.0038(2)	-22.3(09)
	U-C	10(4)	3.45(2)	0.006(5)	
		S_0^2 = 1.0		R(%) = 13.50	

Fig. S13a: Fit results from $U(hfa)_4$. Fitting results compared to data for $U(hfa)_4$ are shown along with resulting fitting parameters. The fitting range is between 1.5 and 4 Å. The k^3 weighted data are transformed between 2.5-14.0 Å^{-1} and are Gaussian narrowed by 0.30 Å^{-1}. The average error per point assuming χ^2 = dof is 0.72. The data have 20.3 independent data points and 14.3 degrees of freedom.

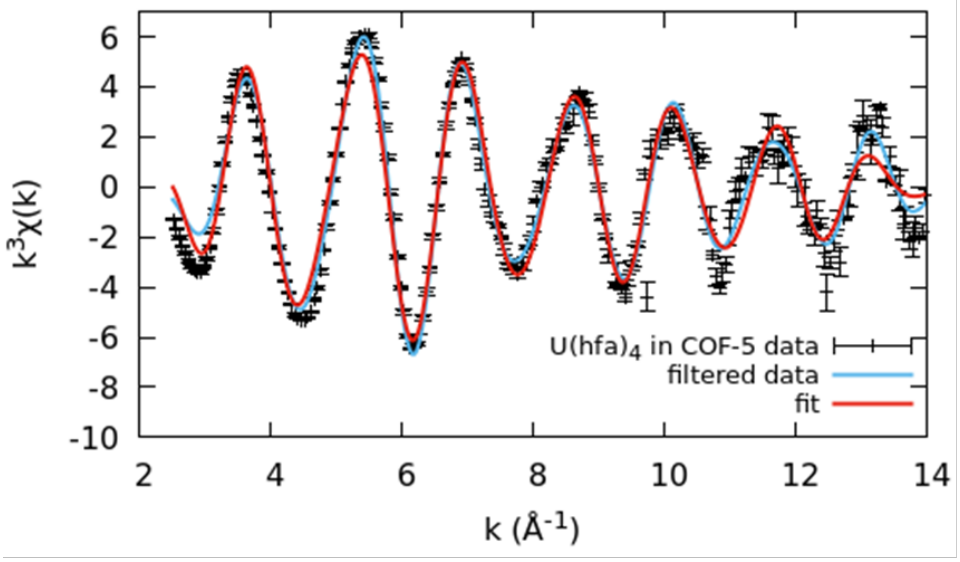

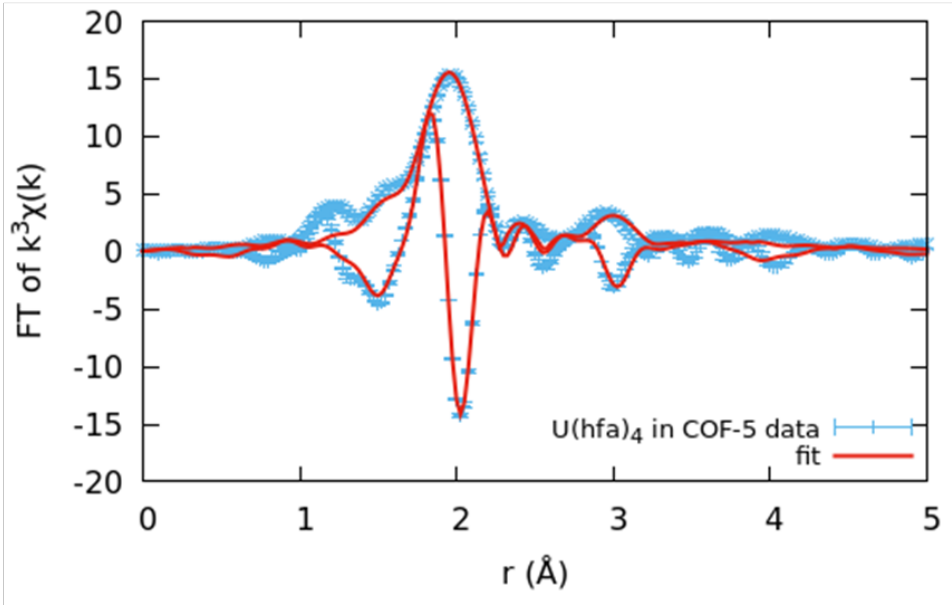

Sample	Path	*N*	*R* (Å)	σ^2 (Å^2)	ΔE_0 (eV)
U(hfa)$_4$@COF-5	U-O	9(1)	2.377(8)	0.0042(7)	-22.5(12)
	U-C	12(4)	3.45(4)	0.010(7)	
	S_0^2 = 0.9			**R(%)** = 17.88	

Fig. S13b: Fit results from U(hfa)$_4$@COF-5. Fitting results compared to data for U(hfa)$_4$@COF-5 are shown along with resulting fitting parameters. The fitting range is between 1.2 and 3.5 Å. The k^3 weighted data are transformed between 2.5-14.0 Å^{-1} and are Gaussian narrowed by 0.30 Å^{-1}. The average error per point assuming χ^2 = dof is 0.97. The data have 18.8 independent data points and 11.8 degrees of freedom.

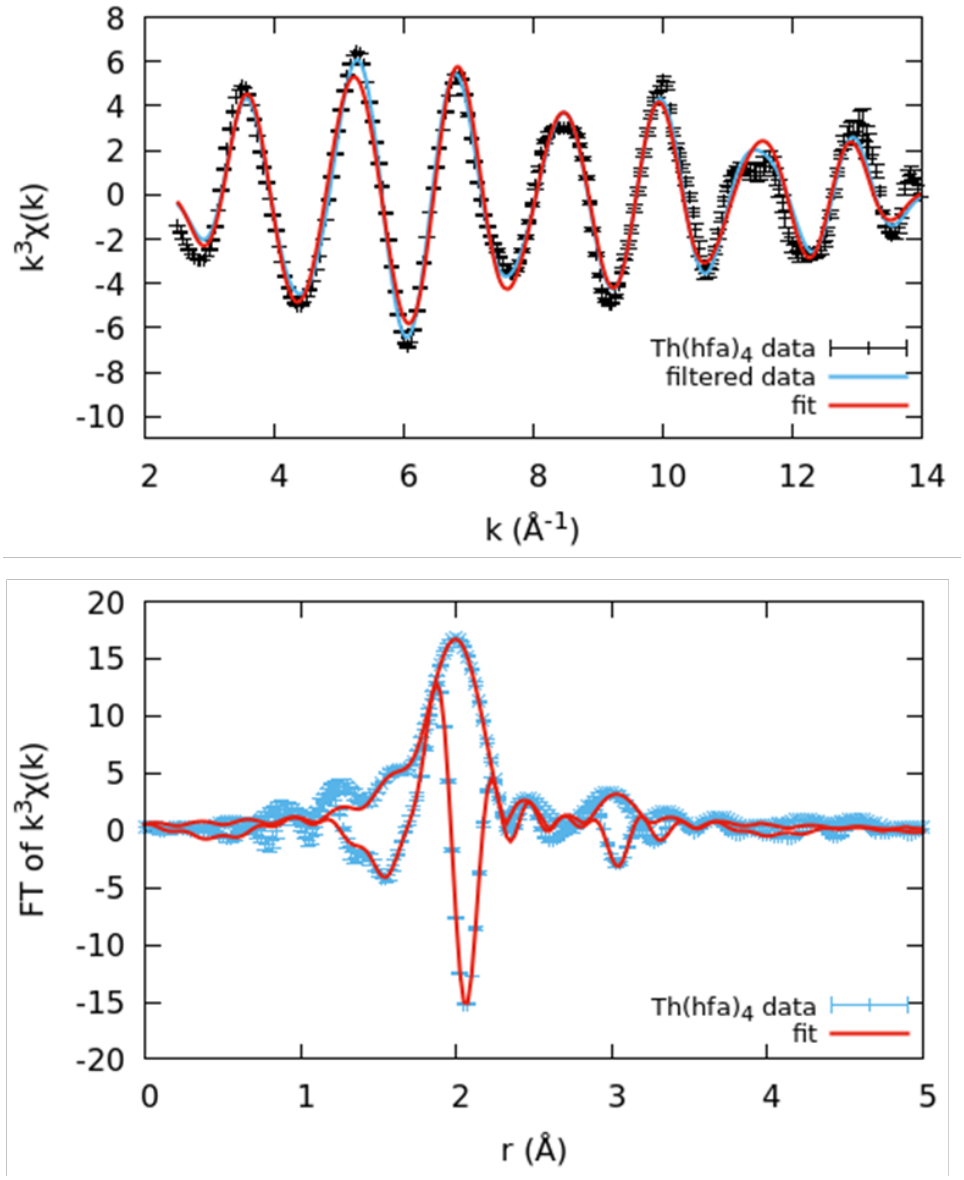

Sample	Path	*N*	*R* (Å)	σ^2 (Å^2)	ΔE_0 (eV)
$Th(hfa)_4$ precursor	Th-O	9(1)	2.443(6)	0.0037(4)	-21.8(7)
	Th-C	6(4)	3.45(3)	0.005(9)	
	S_0^2 = 0.9			**R(%)** = 13.84	

Fig. S13c: Fit results from $Th(hfa)_4$. Fitting results compared to data for $Th(hfa)_4$ are shown along with resulting fitting parameters. The fitting range is between 1.3 and 4 Å. The k^3 weighted data are transformed between 2.5-14.0 Å^{-1} and are Gaussian narrowed by 0.30 Å^{-1}. The average error per point assuming χ^2 = dof is 0.71. The data have 21.8 independent data points and 14.8 degrees of freedom.

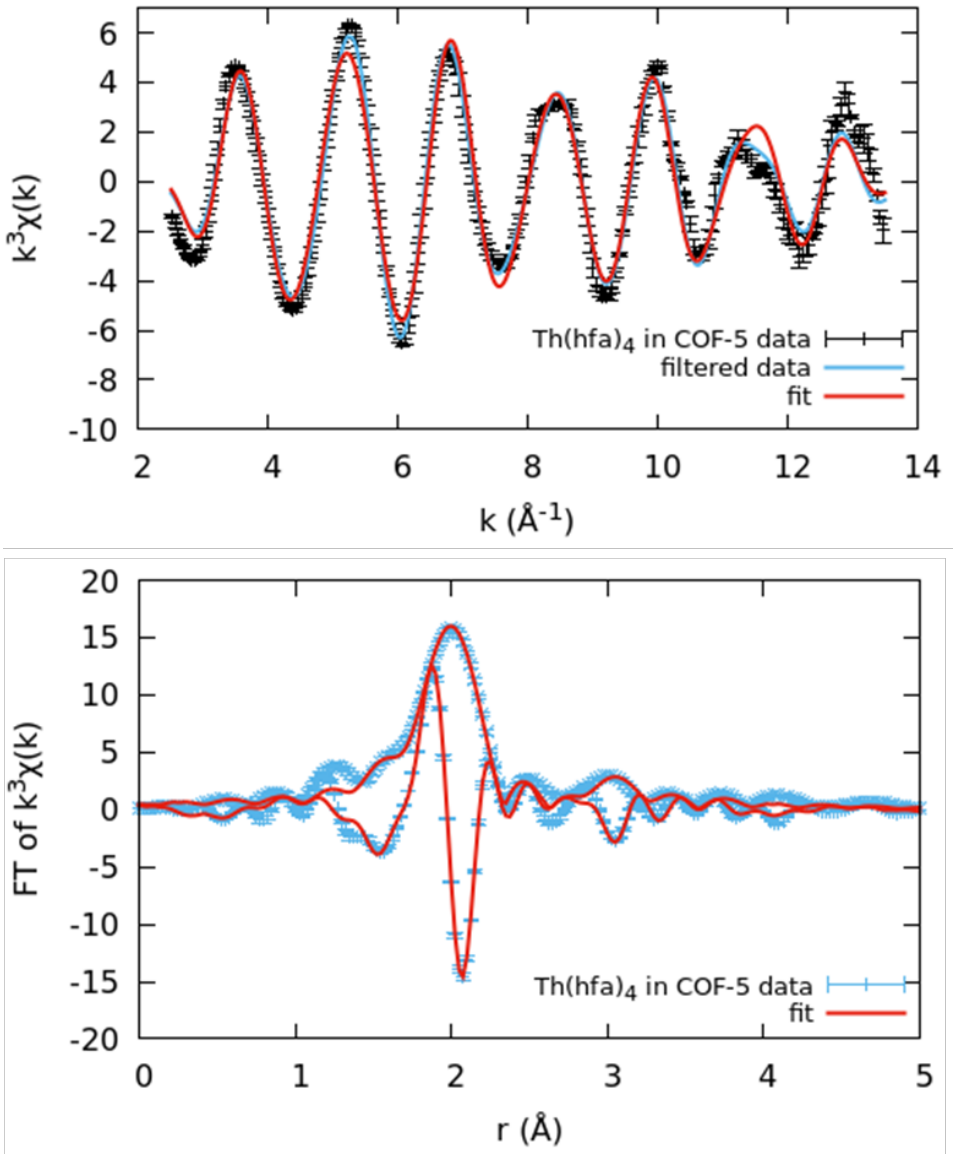

Sample	Path	*N*	*R* (Å)	σ^2 (Å^2)	ΔE_0 (eV)
Th(hfa)$_4$@COF-5	Th-O	9(1)	2.451(7)	0.0043(5)	-22.1(7)
	Th-C	4(3)	3.45(2)	0.001(5)	
	S_0^2 = 0.9			**R(%)** = 14.48	

Fig. S13d: Fit results from Th(hfa)$_4$@COF-5. Fitting results compared to data for Th(hfa)$_4$@COF-5 are shown along with resulting fitting parameters. The fitting range is between 1.3 and 4 Å. The k^3 weighted data are transformed between 2.5-13.5 Å^{-1} and are Gaussian narrowed by 0.30 Å^{-1}. The average error per point assuming χ^2 = dof is 0.72. The data have 20.9 independent data points and 13.9 degrees of freedom.

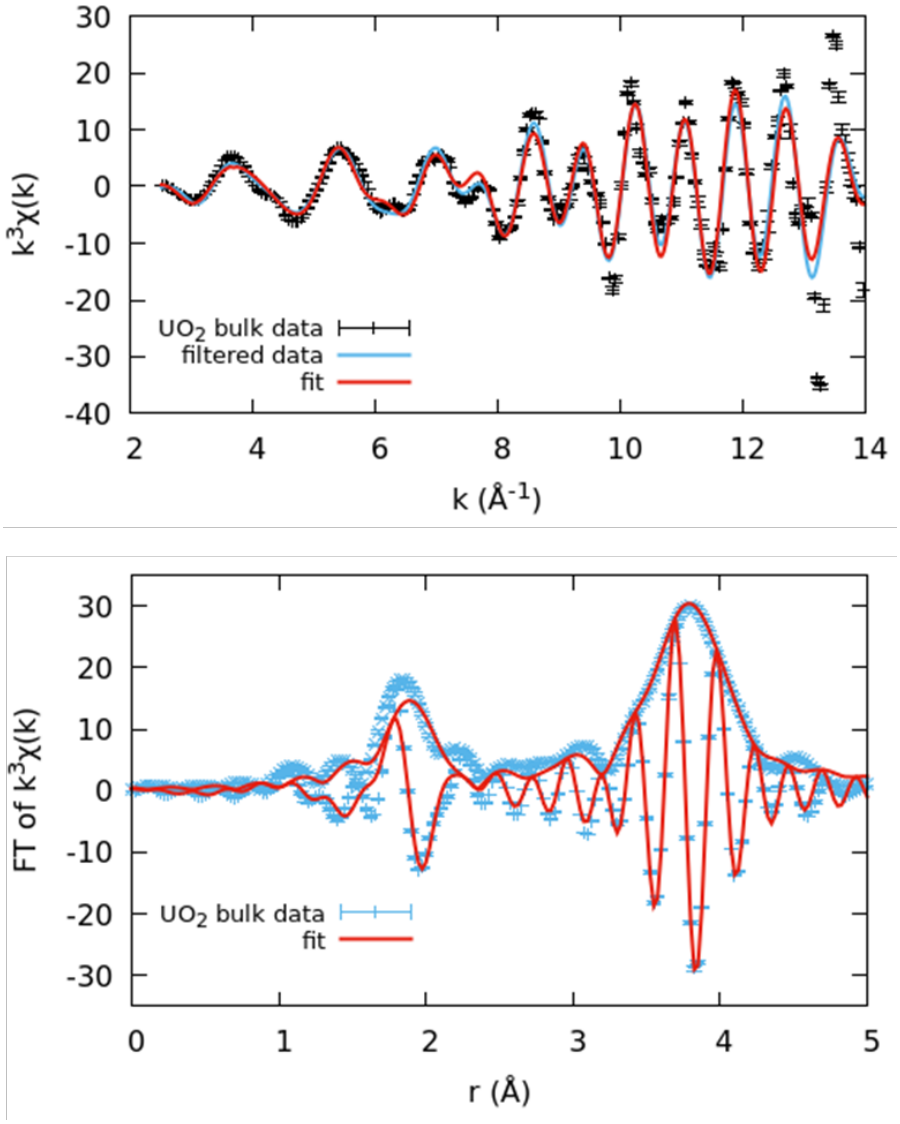

Sample	Path	*N*	*R* (Å)	σ^2 (Å^2)	ΔE_0 (eV)
UO_2 (standard)	U-O	8(1)	2.34(3)	0.005(1)	-15.0(41)
	U-U	12(2)	3.87(1)	0.0013(6)	
	U-O	24(4)	4.49(3)	0.004(6)	
	S_0^2 =	0.935(178)		**R(%)** =	19.7

Fig. S13e: Fit results from bulk UO_2. Fitting results compared to data for UO_2 are shown along with resulting fitting parameters. The fitting range is between 1.4 and 4.5 Å. The k^3 weighted data are transformed between 2.5-14.0 Å^{-1} and are Gaussian narrowed by 0.30 Å^{-1}. The average error per point assuming χ^2 = dof is 2.19. The data have 24.7 independent data points and 16.7 degrees of freedom.

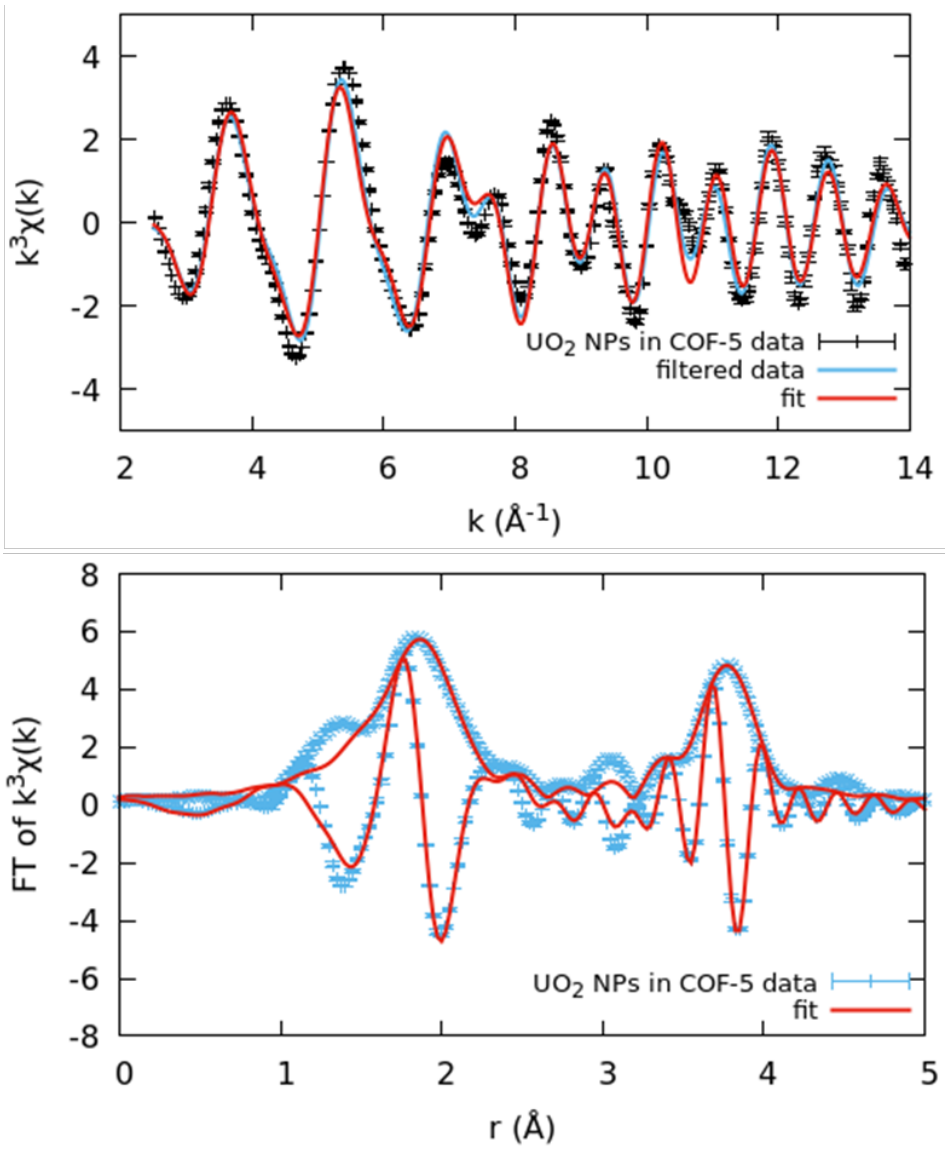

Sample	Path	*N*	*R* (Å)	σ^2 (Å^2)	ΔE_0 (eV)
UO_2 NPs@COF-5	U-O	6(1)	2.34(1)	0.011(1)	-13.6(09)
	U-U	3(1)	3.860(8)	0.004(1)	
	S_0^2 = 0.95			**R(%)** = 15.82	

Fig. S13f: Fit results from UO_2 NPs@COF-5. Fitting results compared to data for UO_2 NPs@COF-5 are shown along with resulting fitting parameters. The fitting range is between 1.4 and 4 Å. The k^3 weighted data are transformed between 2.5-14.0 Å^{-1} and are Gaussian narrowed by 0.30 Å^{-1}. The average error per point assuming χ^2 = dof is 0.4. The data have 21 independent data points and 14 degrees of freedom.

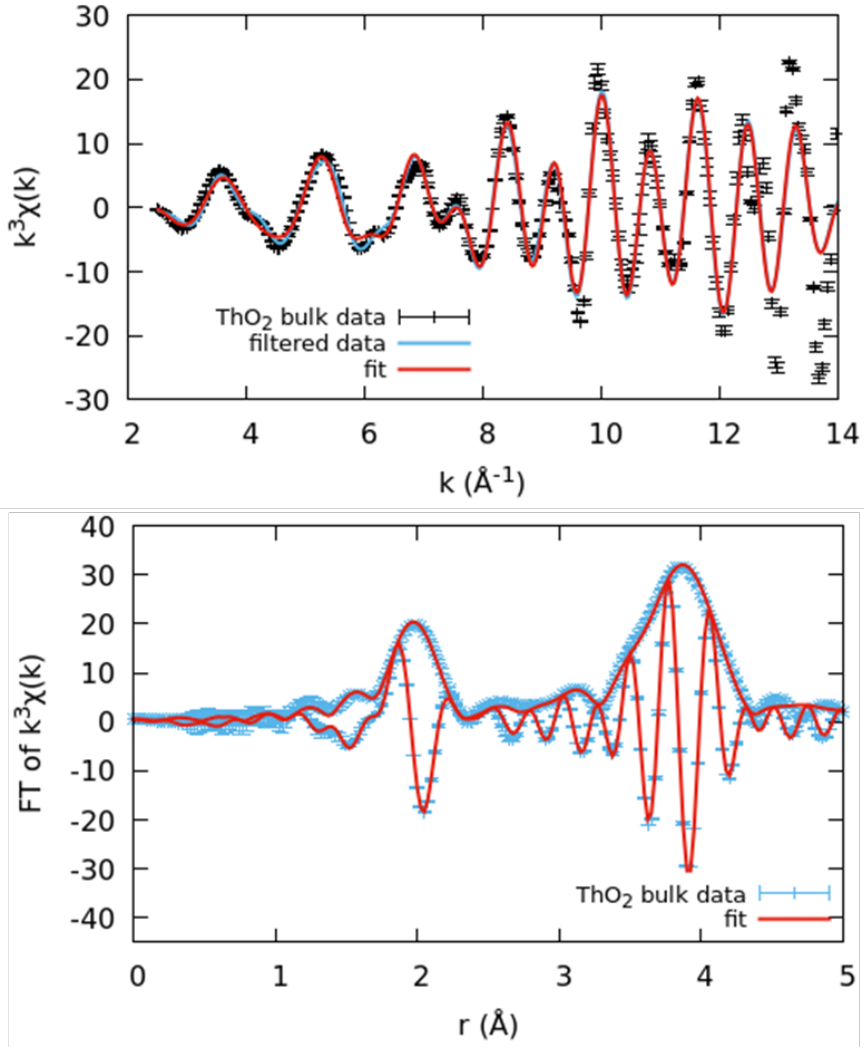

Sample	Path	*N*	*R* (Å)	σ^2 (Å^2)	ΔE_0 (eV)
ThO_2 standard	Th-O	9(1)	2.413(6)	0.0026(6)	-15.0(09)
	Th-Th	13(4)	3.948(5)	0.0005(4)	
	Th-O	19(5)	4.63(2)	0.001(1)	
	ThO_2 MS sink	2(1)	4.38(6)	0.01(2)	
	S_0^2 = 0.94			**R(%)** = 8.46	

Fig. S13g: Fit results from bulk ThO_2. Fitting results compared to data for bulk ThO_2 are shown along with resulting fitting parameters. The fitting range is between 1.5 and 5 Å. The k^3 weighted data are transformed between 2.5-14 Å^{-1} and are Gaussian narrowed by 0.30 Å^{-1}. The average error per point assuming χ^2 = dof is 1.07. The data have 27.6 independent data points and 17.6 degrees of freedom.

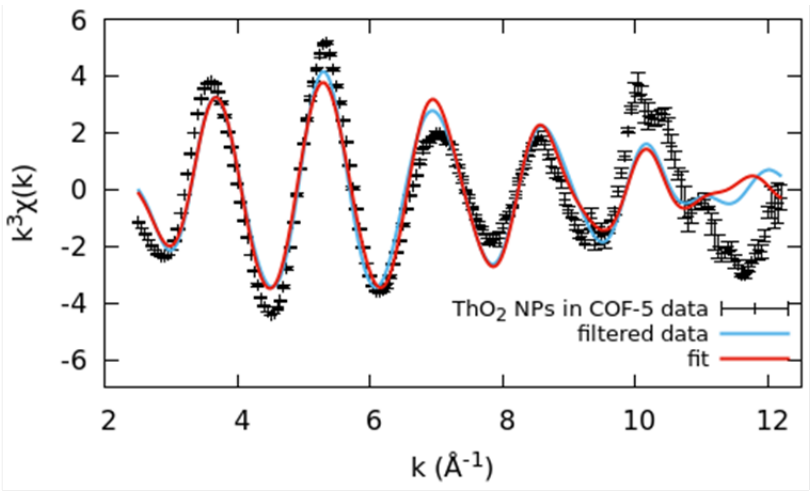

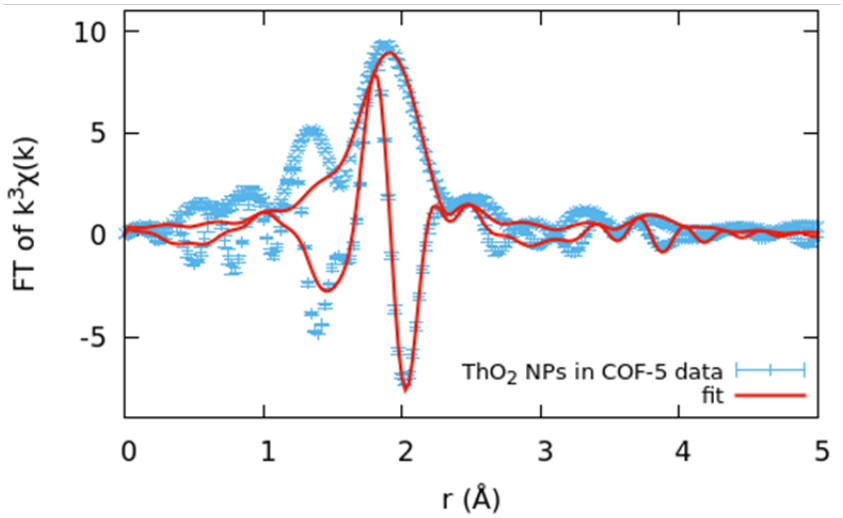

Sample	Path	*N*	*R* (Å)	σ^2 (Å^2)	ΔE_0 (eV)
ThO_2 NPs@COF-5	Th-O	7(1)	2.38(1)	0.008(1)	-13.7(11)
	Th-Th	2(2)	3.891(*)	0.003(6)	
		S_0^2 = 0.95		R(%) = 17.18	

Fig. S13h: Fit results from ThO_2 NPs@COF-5. Fitting results compared to data for ThO_2 NPs@COF-5 are shown along with resulting fitting parameters. The fitting range is between 1.5 and 4 Å. The k^3 weighted data are transformed between 2.5-12.2 Å^{-1} and are Gaussian narrowed by 0.30 Å^{-1}. The average error per point assuming χ^2 = dof is 0.57. The data have 17.4 independent data points and 10.4 degrees of freedom. It should be noted that an error bar on the second shell distance could not be determined. This is likely a result of the nature of this peak, which, while the fit statistics are improved upon including the second shell, it does not pass an F-test. Rather, it has been included for consistency and because the best-fit parameters are reasonable.

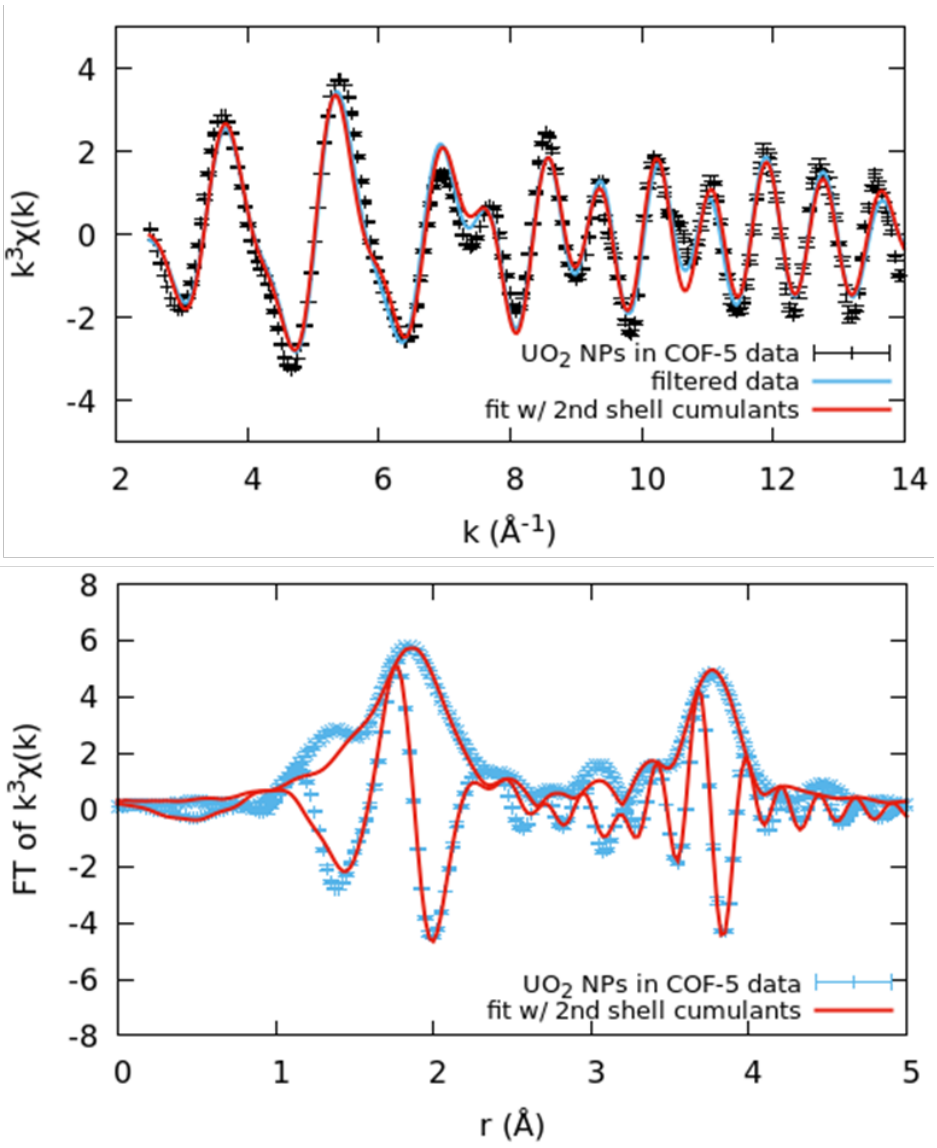

Sample	Path	*N*	*R* (Å)	σ^2 (Å^2)	ΔE_0 (eV)
UO_2 NPs@COF-5	U-O	6(1)	2.34(1)	0.011(1)	-13.5(11)
	U-U	5(3)	3.87(2)	0.009(5)	C_3= 0.00(6), C_4=0.07(4)
	S_0^2 = 0.95			**R(%)** = 14.9	

Fig. S13i: Fit results from UO_2 NPs@COF-5 with 3rd and 4th cumulant included in 2nd shell. Fitting results compared to data for UO_2 NPs@COF-5 are shown along with resulting fitting parameters. The fitting range is between 1.4 and 4 Å. The k^3 weighted data are transformed between 2.5-14.0 Å^{-1} and are Gaussian narrowed by 0.30 Å^{-1}. The average error per point assuming χ^2 = dof is 0.41. The data have 21 independent data points and 12 degrees of freedom.

Temperature-Dependent σ^2 Analysis Using an Einstein Model

Temperature-dependent analysis using an Einstein model was performed in order to determine the amount of static disorder within the samples. This provides both a concept of disorder in the nanoparticle vs bulk structures as well as increased confidence in derived coordination numbers, which are correlated parameters. Derived parameters were determined using an Einstein model in all cases for consistency.[9] It should be noted, however, that when a correlated Debye model was used alternatively, the static disorder extracted was nearly identical to that from the Einstein model, but with higher Debye Temperatures throughout. This is due to the cutoff frequency in the Einstein model, making Einstein temperature lower compared to the Debye temperature by a multiplicative constant.[9, 10] Results of this analysis are summarized in Table 3 of the manuscript.

EXAFS data were collected at four different temperatures (50, 100, 200 and 300 K) and fitting parameters extracted at each of these temperatures in order to obtain σ^2 as a function of temperature. The coordination number determined from the 50 K fit was held fixed to this value at the other temperatures in order to accurately extract σ^2. Results and fitting to an Einstein model are shown below.

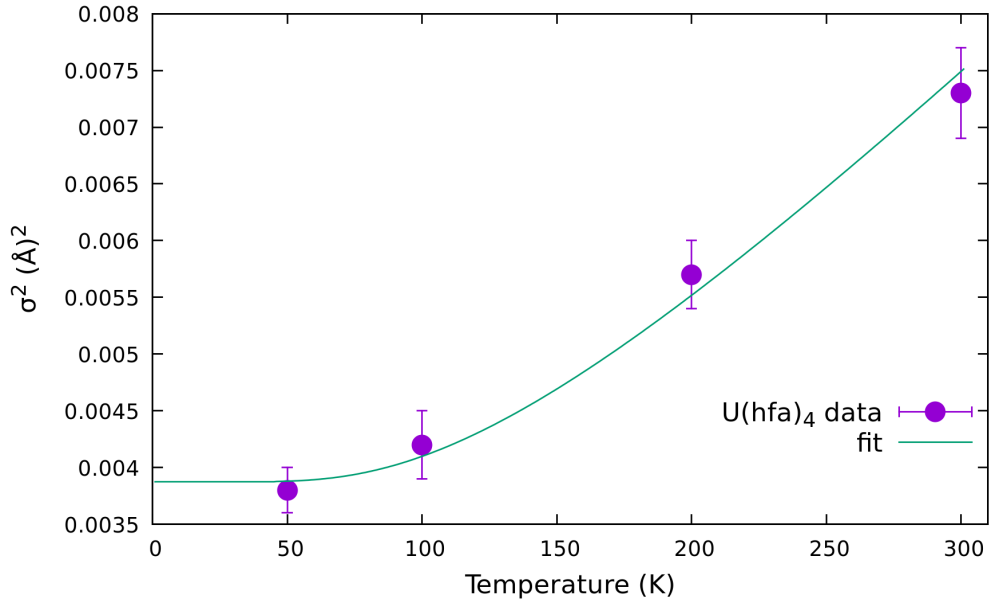

Temperature (K)	σ^2 (Å^2)
50	0.0038 ± 0.0002
100	0.0042 ± 0.0003
200	0.0057 ± 0.0003
300	0.0073 ± 0.0004

Figure S14a: U(hfa)$_4$ temperature dependant fitting results and fit to an Einstein model.

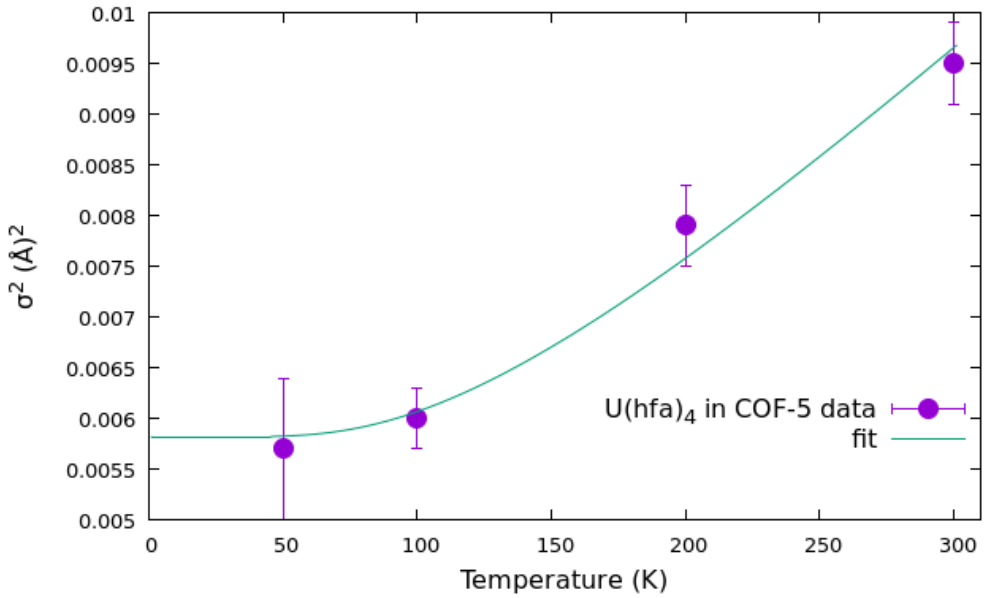

Temperature (K)	σ^2 (Å^2)
50	0.0057 ± 0.0007
100	0.0060 ± 0.0003
200	0.0079 ± 0.0004
300	0.0095 ± 0.0004

Figure S14b: U(hfa)$_4$@COF-5 temperature dependent fitting results and fit to an Einstein model.

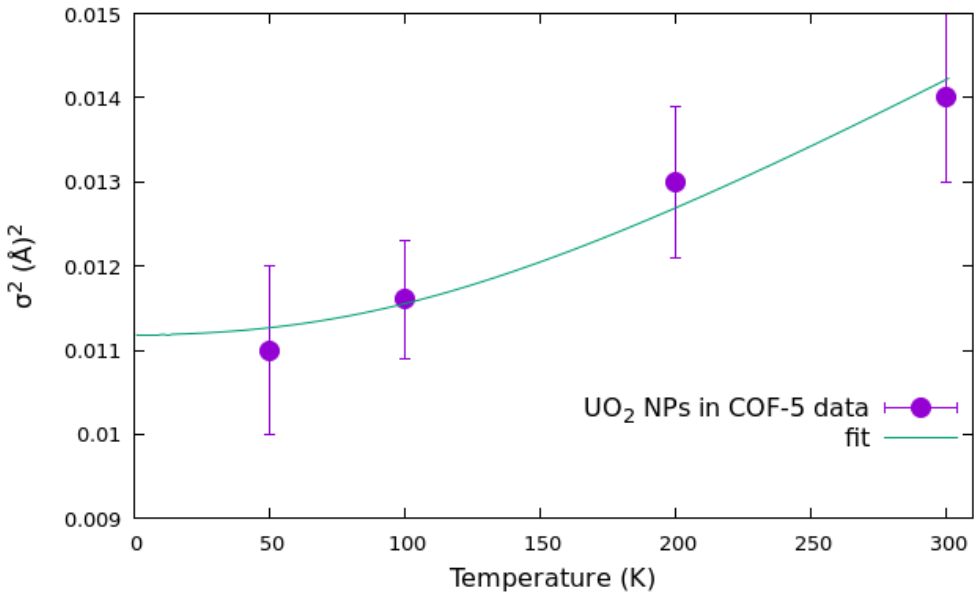

Temperature (K)	σ^2 (Å^2)
50	0.011 ± 0.001
100	0.0116 ± 0.0007
200	0.013 ± 0.0009
300	0.014 ± 0.001

Figure S14c: UO_2 NPs@COF-5 temperature dependent fitting results and fit to an Einstein model.

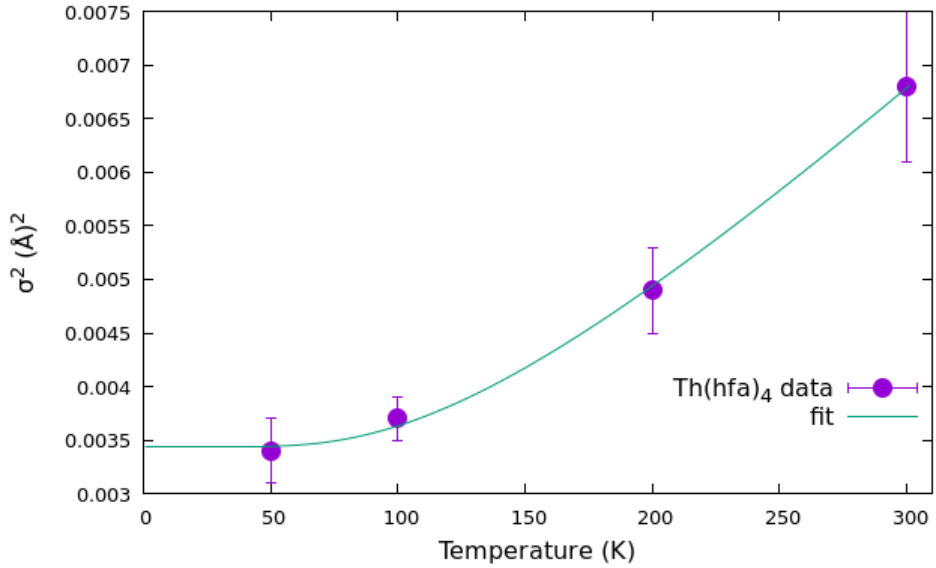

Temperature (K)	σ^2 (Å^2)
50	0.0034 ± 0.0003
100	0.0037 ± 0.0002
200	0.0049 ± 0.0004
300	0.0068 ± 0.0007

Figure S14d: Th(hfa)$_4$ temperature dependent fitting results and fit to an Einstein model.

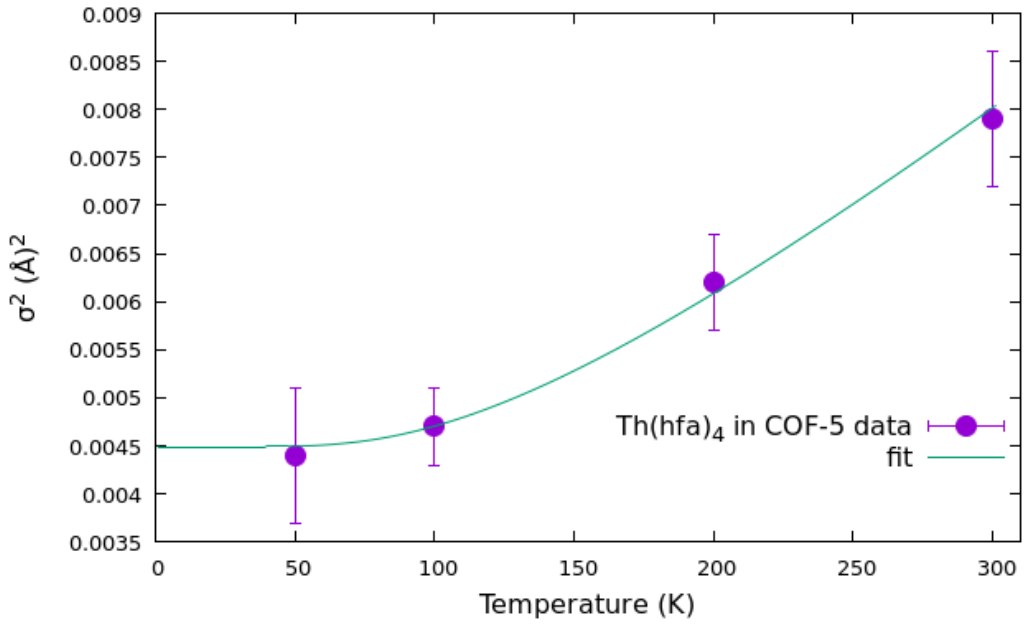

Temperature (K)	σ^2 (Å^2)
50	0.0044 ± 0.0007
100	0.0047 ± 0.0004
200	0.0062 ± 0.0005
300	0.0079 ± 0.0007

Figure S14e: Th(hfa)$_4$@COF-5 temperature dependent fitting results and fit to an Einstein model.

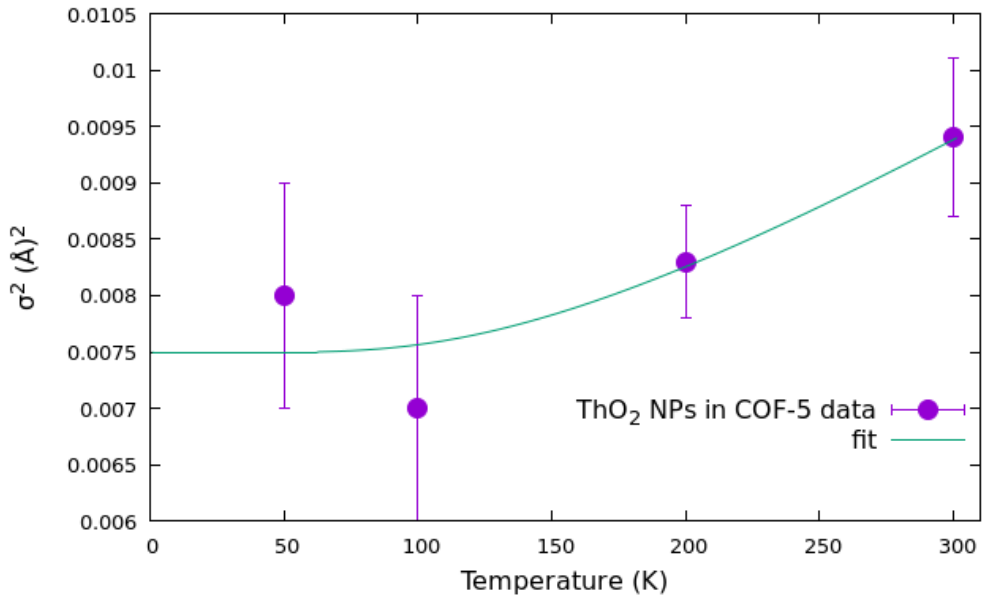

Temperature (K)	σ^2 (Å^2)
50	0.008 ± 0.001
100	0.007 ± 0.001
200	0.0083 ± 0.0005
300	0.0094 ± 0.0007

Figure S14f: ThO_2 NPs@COF-5 temperature dependent fitting results and fit to an Einstein model.

Analysis by method of Calvin et. al

The method developed by Calvin et al[11] was applied to bulk UO_2 and ThO_2 to determine whether or not the decrease in peak intensity for the nanoparticle spectra could be attributed to a decrease in coordination number expected for decreased nanoparticle size (and under-coordinated surface atoms). In Fig. 9 in the manuscript, bulk and nanoscale UO_2 and ThO_2 are shown in comparison to simulations at the nanoparticle sizes determined from STEM (red) and SAXS (blue) using the following equation:

$$N = \left[1 - \frac{3}{4}\left(\frac{r}{R_p}\right) + \frac{1}{16}\left(\frac{r}{R_p}\right)^3\right] N_{bulk}$$

where r is the distance in *r*-space, R_p is the nanoparticle radius and N_{bulk} is the bulk XAFS intensity. It can be seen from Fig. 9 that the nanoparticle spectra have still a lower intensity than simulations based on a decrease in coordination number. Figs. S14-S15 show that to match the decrease in peak intensity observed for the nanoparticles, that a size much lower than that known for the nanoparticles from SAXS is required. As a caveat, it should be noted that the analysis does not account for phase shifts in the resulting plots. The effect may be a ~3% decrease in reality, however this does not affect the observed trends. Therefore, the conclusion is further supported that the decrease in peak intensity is not a result of small nanoparticle size alone, but rather the result of increased disorder compared to bulk.

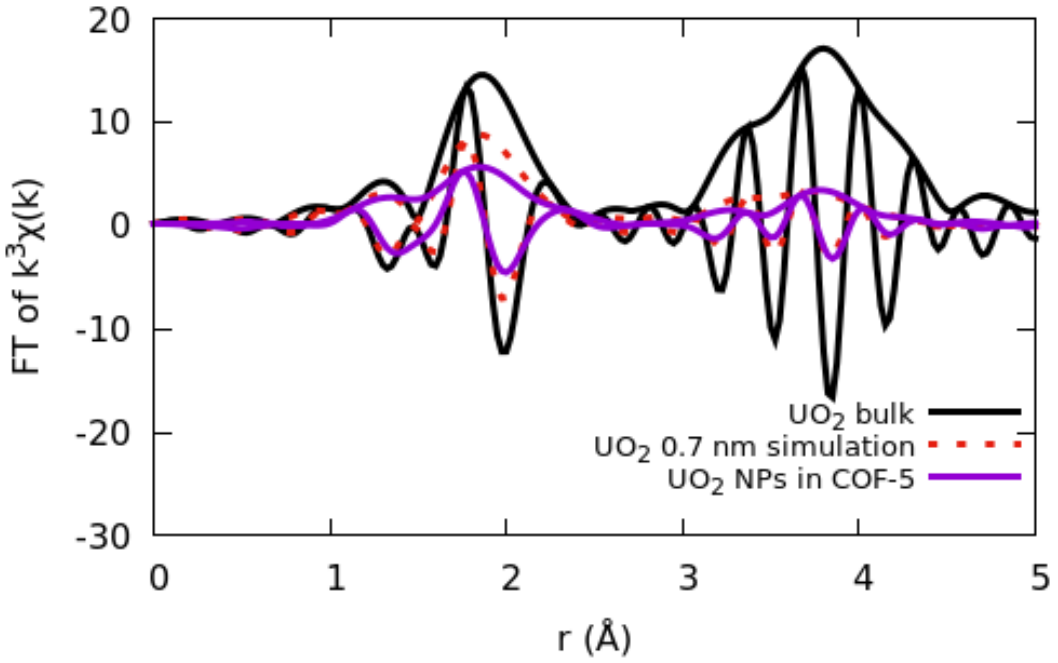

Figure S15: Simulations using method of Calvin et. al for UO_2 NP size required to match experimental spectrum.

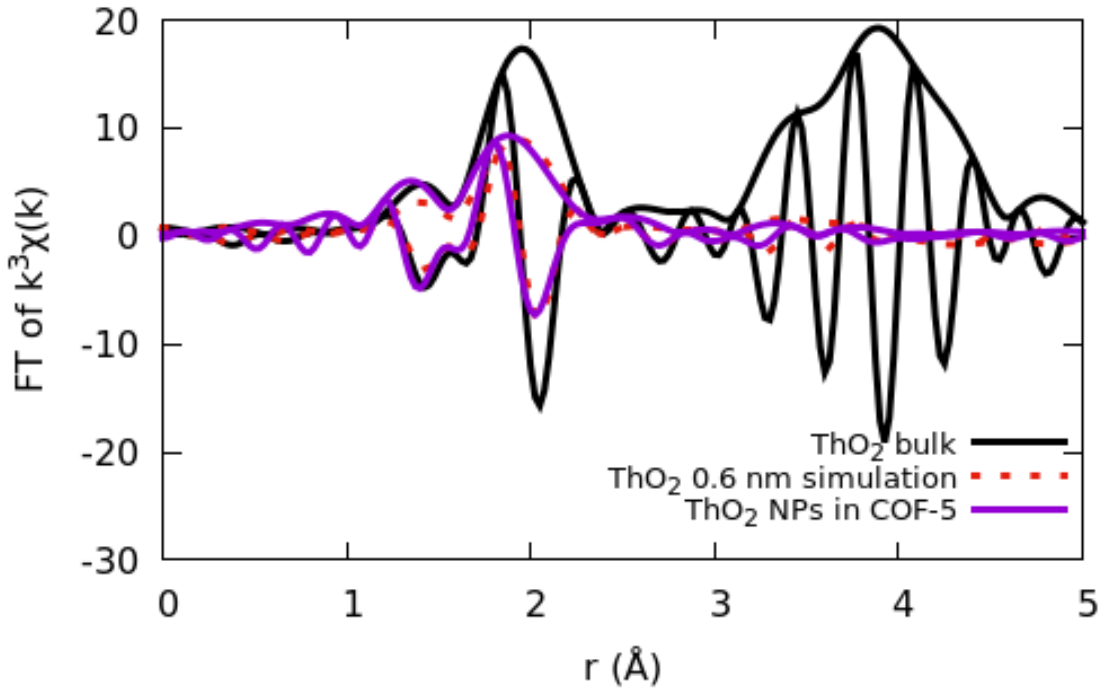

Figure S16: Simulations using method of Calvin et. al for ThO_2 NP size required to match experimental spectrum.

In addition to the above simulations, coordination numbers (CNs) for the first and second shell expected from the equation based on the nanoparticle size from SAXS were compared to those determined from EXAFS fitting. The results are outlined in the table below.

Table S7: Comparison between EXAFS-extracted and Calvin method CNs

Sample	Pathway	CN bulk	CN EXAFS	CN Calvin method
UO_2 NPs@COF-5	U-O (shell 1)	8	6 ± 1	6.0
	U-U (shell 2)	12	3 ± 1	7.0
ThO_2 NPs@COF-5	Th-O (shell 1)	8	7 ± 1	6.2
	Th-Th (shell 2)	12	2 ± 2	7.8

We observe that the coordination numbers expected from the Calvin method match well for the first coordination shell but deviate substantially for the second shell. It should be noted that when 3rd and 4th cumulant are used in fitting the second shell for UO_2 NPs@COF-5 (see Fig. S12i) that the best-fit second shell coordination number matches that expected from the Calvin method within error. Additionally, the Calvin method relies on the assumption that the element of interest is equally distributed on the nanoparticle surface and interior. For oxide particles in particular, where the surface is expected to be oxygenated, it is likely that this is not the case and results may be affected accordingly.

Consideration of a higher order oxide U_xO_y

Our XAFS fitting model for UO_2 NPs@COF-5 uses only two pathways (one for U–O and the other for U–U). Based on the fitting model and following simulations, we evaluate the most likely phase present in the sample and come to the conclusion that UO_2 best describes our nanoparticles. While we cannot entirely rule out the possibility of a minority higher oxide phase being present, evidence suggests that the particles are well described by UO_2 and are therefore referred to as UO_2 rather than UO_{2+x}. Our investigation that led to this conclusion is outlined below:

In order to determine whether or not the decrease in coordination number observed from nanoparticle XAFS fitting compared with bulk UO_2 is the result of a higher oxide contribution, a variety of U_xO_y structures were investigated as alternative candidates to the typical cubic UO_2 structure. This was in part due to the belief that having dangling U bonds would not be expected for such an oxophilic element. In particular, UO_2 in some cases has been noted as UO_{2+x}, where U_3O_8 and phases intermediate to U_3O_8 have often been suspected as impurities.

Structures considered are outlined in Table S8. The first aspect of a reasonable structure to examine is whether or not epitaxial growth is possible. While the nanoparticles are highly disordered, it is still the case that epitaxial growth is generally the energetically favorable case. This would require a relative lattice match of at least one of the lattice parameters with UO_2, given that the nanoparticles can be fit using UO_2 pathways, meaning that the structure must either contain UO_2 or be structurally similar to UO_2. If we compare the lattice parameter for UO_2 to the others listed, the only two structures that have a lattice parameter that is either comparable or comparable to a multiple of the UO_2 lattice parameter are U_4O_9 (5.468 x 4 = 21.872) and U_3O_7 (5.468 x 3 = 16.404). All other structural lattice parameters would be too great a mismatch to enable epitaxial growth- the strain would be too high to be energetically favorable.

Table S8: U_xO_y structures and associated lattice parameters

Structure	space group	a (Å)	b (Å)	c (Å)
UO_2	F m -3 m	5.468	5.468	5.468
α-U_3O_8	C 2 2 2	6.704	11.95	4.142
γ-UO_3	F d d d	9.813	19.93	9.711
U_4O_9	I -4 3 d	21.7666	21.7666	21.7666
U_3O_7	P 4 2/n	12.030	12.030	16.650
U_2O_5	P n m a	6.849	8.274	31.706

The expected local environment for each of the U_xO_y structures was also compared with the nanoparticles and results compiled in Table S9. Given that the average bond length in the

nanoparticles is 2.34 Å, this reveals that the majority structure cannot be α-U_3O_8, γ-UO_3 or U_2O_5, which all have much shorter average bond lengths. UO_2, U_4O_9 and U_3O_7, however, have longer average bond lengths that suggest that they would be better candidates based on this metric. For UO_2, the static disorder should be 0 in an ideal system, given that there is only one U site. The other structures all have multiple U sites which have multiple associated bond lengths. The associated static disorder, that is, the standard deviation of the mean bond length for the multiple pairs, for all other structures actually ends up being higher than that observed for the nanoparticles. This would not be the case were any structure besides UO_2 the majority structure, since in nanoparticles, greater static disorder than bulk is typically observed as a result of amorphous-like surface layers. This suggests that UO_2 is the majority phase present in the nanoparticle samples.

In addition, coordination numbers were calculated by averaging over U sites. Unfortunately, it seems that the only structures with coordination numbers within error of the nanoparticle case have short, prohibitive bond lengths and high static disorder. It is possible that increased static disorder from involvement of another oxide structure may play a role; however each of the aforementioned structural attributes still suggest that the structure is majority UO_2. Due to the decreased coordination number, bond length match and lower static disorder (which is only ~0.005 $Å^2$ if we eliminate the shorter bond lengths in a couple of the U sites), U_3O_7 or possibly U_4O_9 would be the best overall higher oxide to consider as a potential structure. This case is further investigated through simulations to follow.

Table S9: U_xO_y expected local structure parameters

structure	average CN	average bond length U-O (Å)	static disorder ($Å^2$)
NPs*	6 ± 1	2.34 ± .01	0.007 ± 0.001
UO_2	8	2.368	0
α-U_3O_8	6.7	2.19	0.016
γ-UO_3	6	2.12	0.046
U_4O_9	8.1	2.40	0.031
U_3O_7	7.5	2.35	0.016
U_2O_5	6	2.17	0.039

*parameters for the NPs determined through XAFS modeling. The others are determined from theoretical bulk structure.

Using a correlated-Debye temperature of 50K and defining the Debye temperature as T_{cD}=450 K, simulations of various U_xO_y structures were calculated using FEFF, with a cluster radius of 7 Å. In order to test the reasonability of these simulations and choice of T_{cD}, experimental and simulated bulk UO_2 (black and red, respectively) spectra are shown in figure S17 along with the NP@COF-5 spectrum. From this, we observe that the simulated and experimental spectra match

relatively well and exhibit the bond lengths and overall characteristics that are seen in the nanoparticle UO_2. The key significant difference is the diminished intensity of all the peaks in the nanoparticle spectrum.

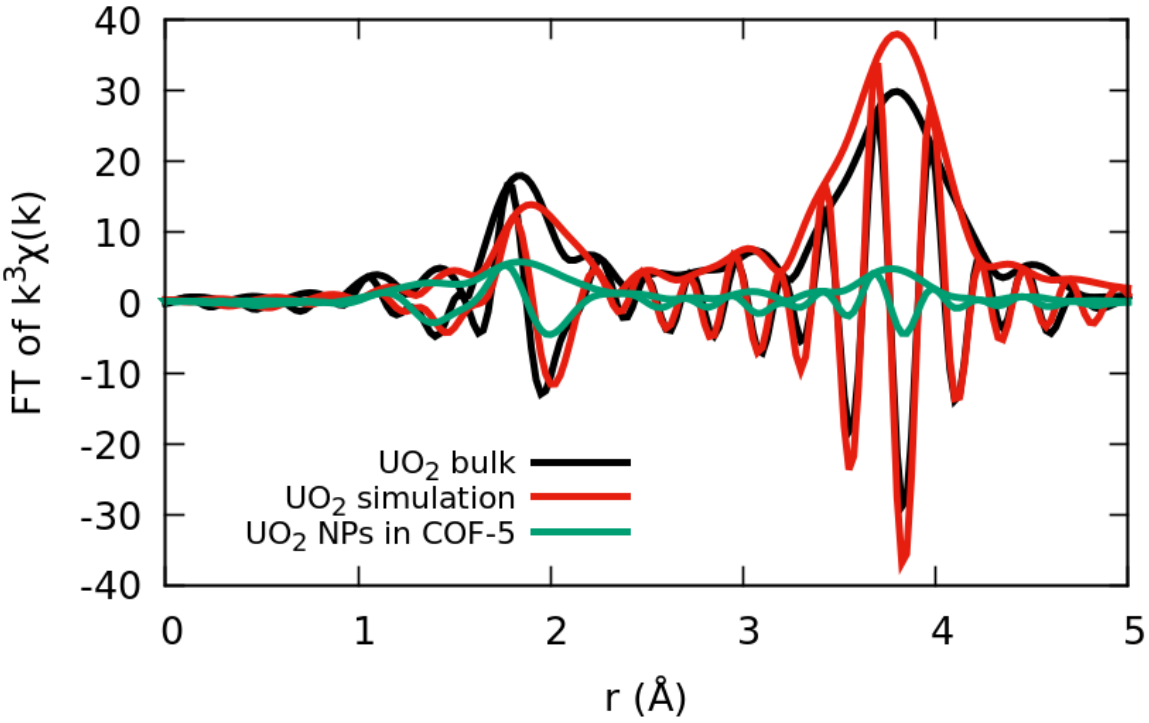

Figure S17: UO_2 experimental and simulated spectra compared to nanoparticle sample spectrum.

In addition to UO_2, three other U_xO_y simulations were compared to the nanoparticle spectrum. α-U_3O_8 was investigated, given its low average coordination number and the fact that it has previously been reported as an oxidation product of UO_2. Results are shown in Figure S18. Although there is some overlap in the peak positions and an overall lowered relative intensity compared to UO_2, the peak shapes and positions make it clear that while we cannot entirely rule out the presence of trace U_3O_8, it does not match as well as does UO_2 and is not a primary phase observed in the nanoparticle spectrum.

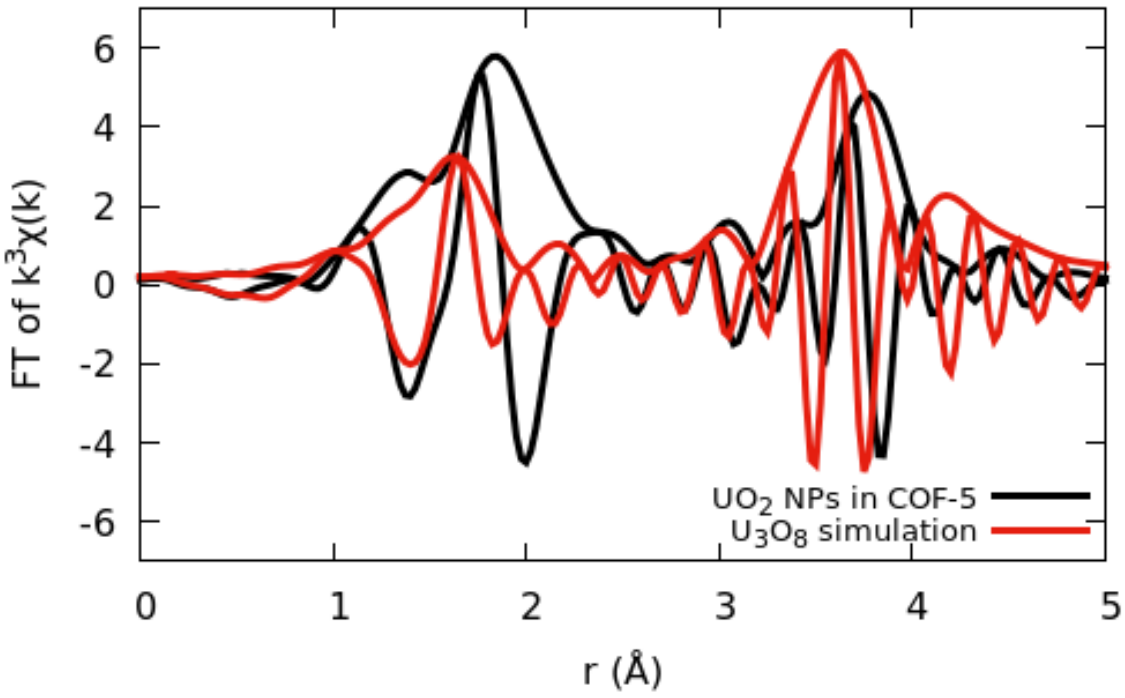

Figure S18: α-U_3O_8 simulation (red) compared to nanoparticle spectrum (black).

Simulations of U_4O_9 and U_3O_7 were also run and are compared with the nanoparticle spectrum in figures 10 and S19, respectively. These two structures show the greatest agreement besides UO_2 based on their lattice parameter match and average bond length. We observe that both structures (and in particular U_3O_7) show some similarity to the nanoparticle spectra, but with greater disorder than is observed for the nanoparticles, particularly in the first shell. Presence of either of these phases may be able to explain the higher radial disorder and lowered intensity observed in the case of the nanoparticles in comparison to bulk UO_2; however, from the peak shapes and relative intensities observed, it is still clear that the nanoparticles are in majority disordered UO_2 based on these results.

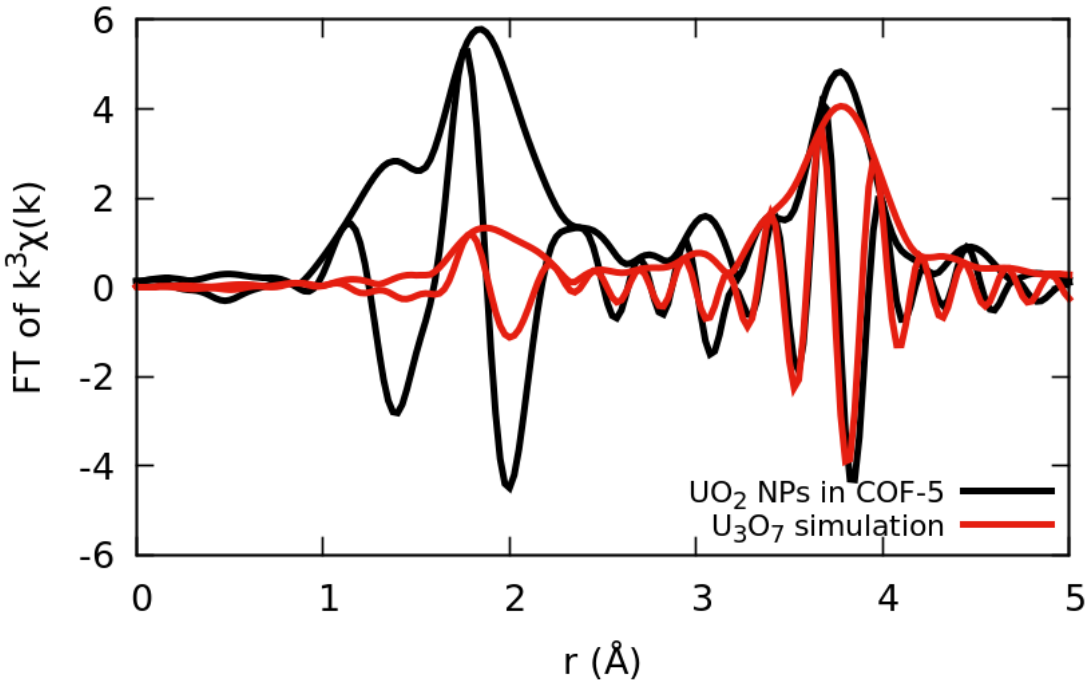

Figure S19: U_3O_7 simulation (red) compared to NP spectrum (black).

This hypothesis is further supported by XANES simulations using FEFF (figure S20). A cluster radius of 7 Å was used as well as the SCF (self-consistent field) card. While presence of U_3O_7 in particular may in part explain the lack of a post-edge shoulder observed in bulk UO_2 but not in the nanoparticles, this cannot describe the increased white line intensity. Actually, experimental UO_{2+x} spectra have in contrast shown a lowered white line intensity compared to UO_2.[12] In addition, an edge shift to higher energy compared to bulk UO_2 is not observed in the nanoparticles, whereas it is in the higher oxide simulated spectra. This suggests that the increased white line is due to a size confinement effect and not due to the presence of secondary phases. Thus, while we cannot rule out the presence of a higher oxide, it is clear that UO_2 is the majority phase present in the nanoparticles, which can therefore be best described as UO_2 nanoparticles.

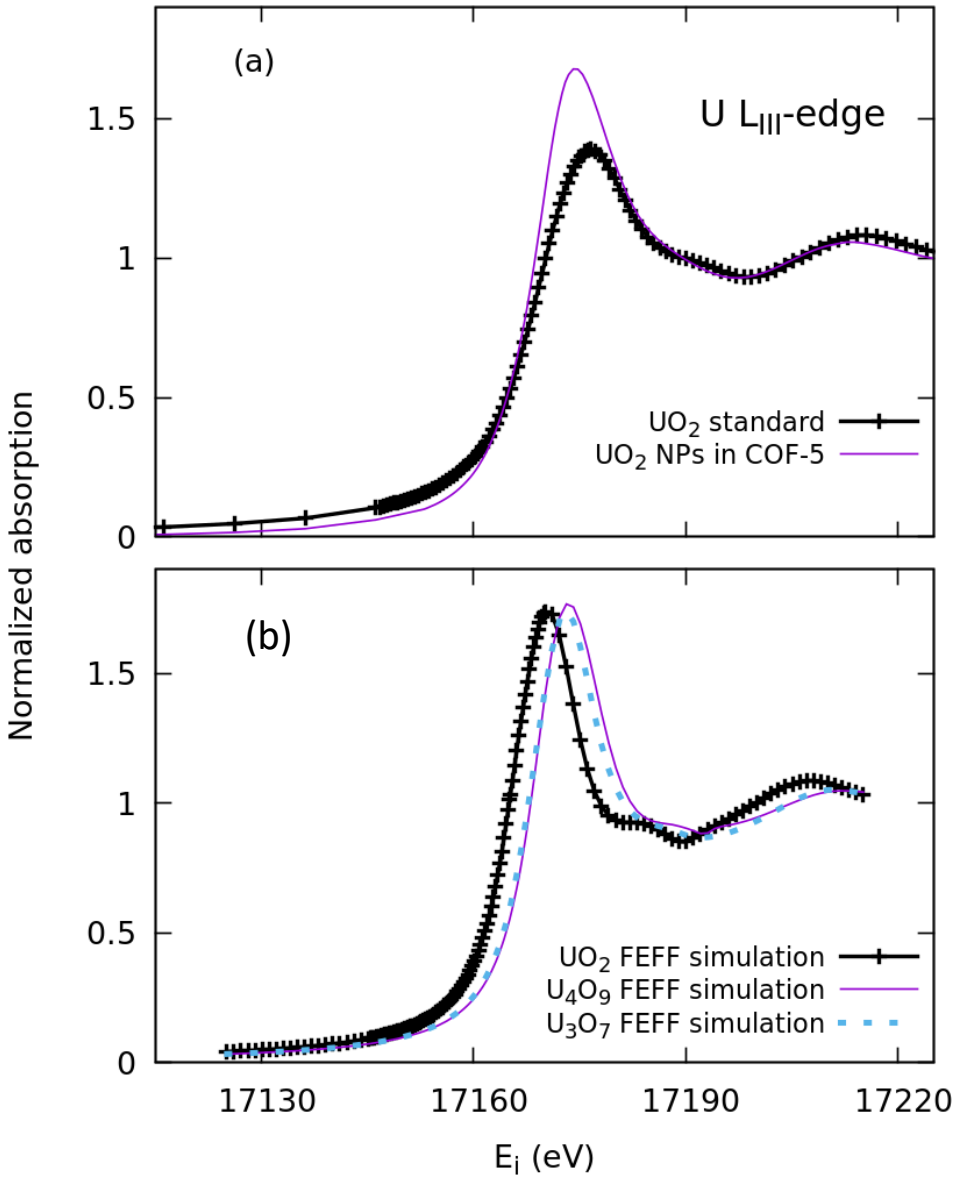

Figure S20: XANES experimental spectra (a) of UO_2 bulk and nanoparticles compared with FEFF simulations (b) of relevant U_xO_y structures.

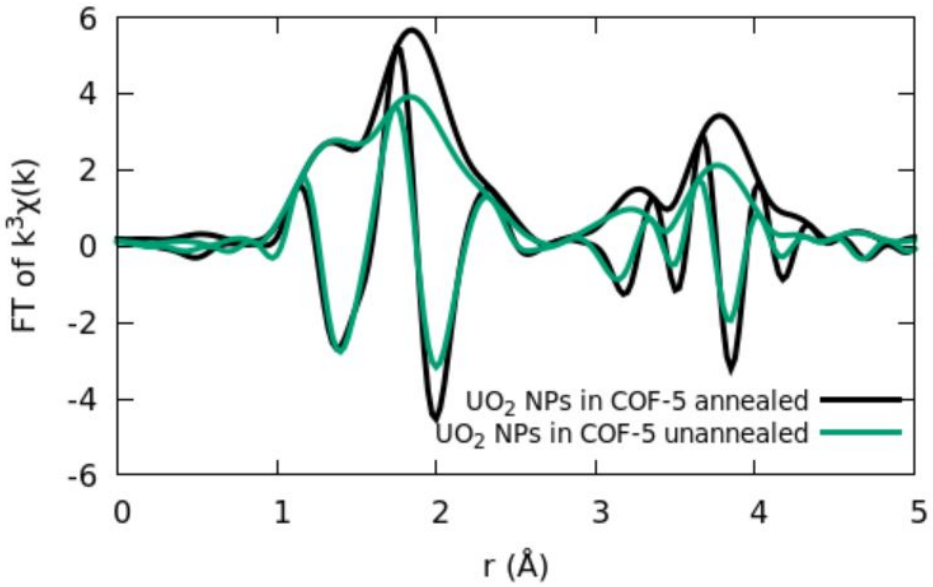

Figure S21: Comparison of UO_2 NPs@COF-5 before and after annealing in H_2.

Figure S21 shows that UO_2 NPs@COF-5 prior to heating under H_2 at 300 °C appear similar to after this annealing step, with the exception of a change in EXAFS peak amplitude. This difference can be attributed to the increased crystallinity in the annealed sample (black) compared to the sample prior to annealing (teal). No evidence of peaks from a higher uranium oxide are present, suggesting that the annealing step plays no role in changing the phase or composition of the resulting product.

References

1. *APEX3, SADABS, and SAINT*, Bruker XAS: Madison, WI, USA.

2. G. M. Sheldrick, *Acta Cryst.*, 2015, **71**, 3-8.

3. L. J. Farrugia, *J. Appl. Cryst.*, 2012, **45**, 849-854.

4. M. Kotlarchyk and S. H. Chen, *J. Chem. Phys.*, 1983, **79**, 2461-2469.

5. V. L. Devito and D. W. Wester, *J. Inorg. Nucl. Chem.*, 1980, **42**, 1719-1723.

6. A. P. Cote, A. I. Benin, N. W. Ockwig, M. O'Keeffe, A. J. Matzger and O. M. Yaghi, *Science*, 2005, **310**, 1166-1170.

7. R. Lessard, J. Cuny, G. Cooper and A. P. Hitchcock, *Chem. Phys.*, 2007, **331**, 289-303.

8. G. J. P. Deblonde, T. D. Lohrey, C. H. Booth, K. P. Carter, B. F. Parker, Å. Larsen, R. Smeets, O. B. Ryan, A. S. Cuthbertson and R. J. Abergel, *Inorg. Chem.*, 2018, **57**, 14337-14346.

9. E. D. Crozier, J. J. Rehr and R. Ingalls, in *X-Ray Absorption: Principles, Applications, Techniques of EXAFS, SEXAFS, XANES*, eds. D. Konginsberger and R. Prins, Wiley, New York, 1988, ch. 373, p. 373.

10. E. Sevillano, H. Meuth and J. J. Rehr, *Phys. Rev. B*, 1979, **20**, 4908-4911.

11. S. Calvin, M. M. Miller, R. Goswami, S.-F. Cheng, S. P. Mulvaney, L. J. Whitman and V. G. Harris, *J. Appl. Phys.*, 2003, **94**, 778-783.

12. S. D. Conradson, B. D. Begg, D. L. Clark, C. den Auwer, M. Ding, P. K. Dorhout, F. J. Espinosa-Faller, P. L. Gordon, R. G. Haire, N. J. Hess, R. F. Hess, D. Webster Keogh, G. H. Lander, D. Manara, L. A. Morales, M. P. Neu, P. Paviet-Hartmann, J. Rebizant, V. V. Rondinella, W. Runde, C. Drew Tait, D. Kirk Veirs, P. M. Villella and F. Wastin, *J. Solid State Chem.*, 2005, **178**, 521-535.